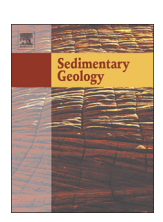
ELSEVIER

Contents lists available at ScienceDirect

# Sedimentary Geology

journal homepage: www.elsevier.com/locate/sedgeo



# Quantifying paleoecological impact of the OAE1a on shallow marine ecosystems from southeastern France



Alexis Godet a,\*, Jacob Byerly a,b, Matthew Bourdon a,c, Marina Suarez d

- <sup>a</sup> Department of Earth and Planetary Sciences, The University of Texas at San Antonio, San Antonio, TX, USA
- <sup>b</sup> EOG Resources, Corpus Christi, TX, USA
- <sup>c</sup> Petrotek Engineering Corporation, Littleton, CO, USA
- <sup>d</sup> Department of Geology, The University of Kansas, Lawrence, KS, USA

#### ARTICLE INFO

Article history:
Received 13 August 2024
Received in revised form 7 October 2024
Accepted 7 October 2024
Available online 11 October 2024

Editor: Dr. Catherine Chagué

Keywords: Early Cretaceous Aptian Geochemistry Point counting analysis Statistical analysis

#### ABSTRACT

Climate and environmental instability during the early Aptian culminated with the unfolding of the Oceanic Anoxic Event (OAE) 1a, which resulted in the deposition of black shales in deep marine settings and a typical negative spike followed by a positive excursion in  $\delta^{13}$ C values. In Vercors (southern France) the Urgonian platform developed prior to and coeval to the OAE1a, but the impact of this paleoenvironmental crisis on the ecology of benthic ecosystems is yet to be quantified. We gathered field and petrographic data to identify sequence boundaries and maximum flooding surfaces that are biostratigraphically dated and correlated between four localities within the study area, A composite  $\delta^{13}$ C curve is built where the C3 to C7 isotope segments from the literature are identified, pinpointing the onset of the OAE1a above the last episode of deposition of Urgonian facies rich in rudist bivalves. Furthermore, thin section point counting data are used to quantify the proportion of allochems in samples and to trace changes in the ecology of ecosystems. The principal component analysis of point counting data helps define ecological tiers: a diversified, photozoan association with rudists, green algae, and benthic foraminifera dominated ecosystems before the OAE1a and up to the C7 segment, while a less diversified heterozoan association with bryozoans and crinoids developed after the OAE1a. To explore the triggers for this change, the principal component analysis of elemental geochemical data highlights an increased nutrient and detrital input as major triggering mechanisms for ecological adjustments and changes in the biodiversity of ecosystems. In particular after the OAE1a, an increase in detrital and nutrient input leads to the replacement of photozoan by heterozoan assemblages more adapted to these stressful conditions. This research directly links paleoenvironmental deterioration to paleoecological changes and quantifies the amount of adaptation of ecosystems.

© 2024 Elsevier B.V. All rights are reserved, including those for text and data mining, Al training, and similar technologies.

## 1. Introduction

The Early Cretaceous (ca. 143 to 100.5 Ma; Gradstein et al., 2020) recorded a strong increase in biodiversity in shallow-marine settings: rudist bivalves radiated from the Valanginian to the Late Cretaceous (Pomar and Hallock, 2008; Skelton and Gili, 2012) while benthic foraminifera colonized environments from the coastline to distal parts of continental shelves (Morard et al., 2022). The disposition of continental landmasses between the tropics and a warmer climate allowed diversified ecosystems to thrive and to produce carbonate series in broad intertropical epicontinental seas (Philip, 2003). Facies analysis of tropical carbonates allows differentiation of two fossil assemblages. According to Föllmi et al. (2006) corals, rudists, benthic foraminifera, and green algae are typical of a photozoan assemblage that flourishes

\* Corresponding author. E-mail address: alexis.godet@utsa.edu (A. Godet). in oligotrophic to slightly mesotrophic waters with lower nutrients and higher oxygen concentrations. However more recent studies report that rudists fed from various forms of organic matter in suspension in the water column, thus not requiring the presence of photosymbionts (Pomar and Hallock, 2008; Steuber et al., 2023). During times of enhanced nutrient supply or cooler temperature, a heterozoan assemblage develops with bryozoans, crinoids and macroalgae. In case of strong nutrient supply or detrital input, carbonate ecosystems may experience choking and enter a phase of drowning when carbonate production is strongly reduced and replaced, for instance, by condensation and authigenesis (Lees and Buller, 1972; Carannante et al., 1988; James, 1997; Mutti and Hallock, 2003; Schlager, 2005; Föllmi et al., 2006; Godet, 2013).

The evolution of shallow-marine carbonate ecosystems is punctuated by periods of slowdown and even shutdown, and the identification of the mode of carbonate production in the rock record allowed previous studies to link major paleoceanographic perturbations to paleoecological

changes on the platform. Föllmi et al. (2006) recognized those phases of drowning of the Helvetic platform during the Valanginian, late Hauterivian-early Barremian, and early Aptian. During the early Aptian, enhanced volcanism released isotopically light carbon dioxide and perturbed the global carbon cycle, leading to the preservation of organic-rich deposits in (hemi)pelagic settings during the unfolding of the Oceanic Anoxic Event (OAE) 1a (Schlanger and Jenkyns, 1976), and to characteristic changes in the carbon isotope composition ( $\delta^{13}$ C) of organic and inorganic carbon. Meanwhile carbonate platforms experienced ecological reorganization (Skelton and Gili, 2012). In the Basque-Cantabrian region of Spain, photozoan assemblages with rudists and corals are replaced by heterozoan associations with bryozoans and crinoids, while pelagic faunas are preserved in a condensed interval related to the OAE1a (Millán et al., 2009; Najarro et al., 2011). Similarly Huck et al. (2012) related the onset of the OAE1a to the widespread bloom of Bacinella/Lithocodium, and concluded that enhanced atmospheric pCO<sub>2</sub> favored continental weathering and the transfer of nutrients to the ocean that stimulated microencruster productivity. Huck et al. (2014) synthesized the impact of the OAE1a on various peri Tethyan and proto North-Atlantic carbonate platforms: photozoan assemblages either transitioned toward a more adapted ecosystem dominated by a mesotrophic assemblage, orbitolinids, or Bacinella/Lithocodium, or remained the same. In the Gargano Promontory of southeastern Italy, Del Viscio et al. (2021) conclude that monospecific accumulation of Chodondrota marked the deterioration of environmental conditions directly prior the OAE1a, that favor the installation of an ecosystem dominated by orbitolinids and Bacinella/Lithocodium. Although the impact of the OAE1a on shallow-marine ecosystems is well established, the character and intensity of the ecological shift in benthic ecosystems are yet to be quantified.

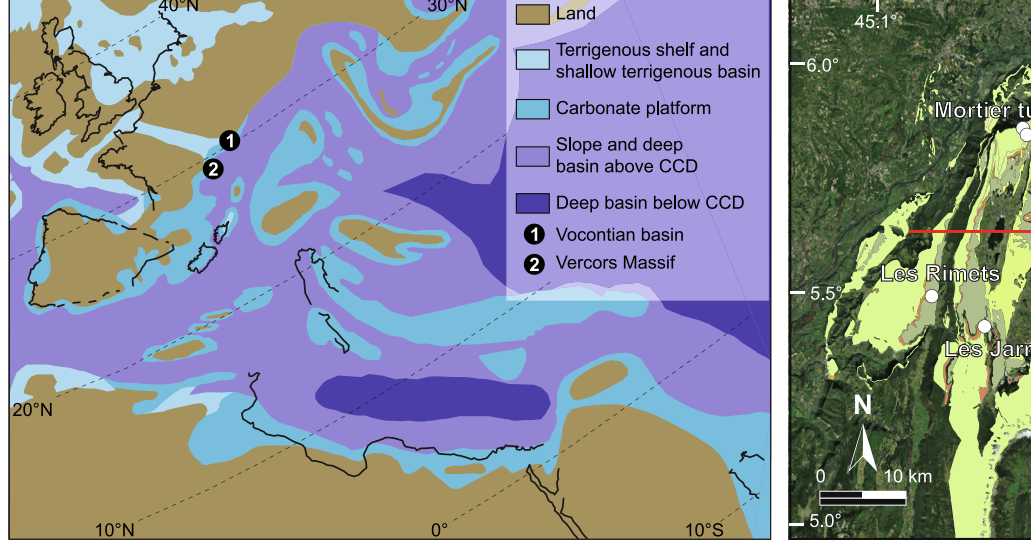
This contribution aims to identify the record of the OAE1a in sedimentary series from the Vercors region of southern France (Fig. 1) using the  $\delta^{13}\text{C}$  value of rock samples. Systematic point counting analysis of thin sections will inform on the paleoecology of ecosystems that thrived in that region of northern Tethys, while elemental geochemistry will be used to assess paleoenvironmental conditions. Our objectives are to evaluate petrographic and geochemical datasets using principal component analysis (PCA) to identify paleoecological associations and paleoenvironmental forcing mechanisms, respectively. We will test the hypothesis that the unfolding of the OAE1a led to a minor shift from a photozoan assemblage to a better adapted, heterozoan

ecosystem but that major paleoecological changes were triggered by enhanced nutrient and detrital supply after the OAE1a.

#### 2. Geological setting

During the Early Cretaceous the Vercors was located on the northern margin of the Tethys Ocean (Fig. 1) where a broad carbonate platform developed (Masse et al., 1993; Arnaud, 2005b). A warm climate and tectonically-enhanced local subsidence favored the accumulation of carbonate shallow-marine deposits (Arnaud, 2005b; O'Brien et al., 2017). On top of Hauterivian hemipelagic deposits the Glandasse Bioclastic Limestone, the Urgonian Limestone (rudist-bearing formation divided into a lower and an upper member by the Lower Orbitolina Beds), and the Upper Orbitolina Beds (bioclastic limestone with a higher content in large benthic foraminifera) were deposited (e.g., Arnaud-Vanneau and Arnaud, 1990). Following on top the Lumachelle I and Lumachelle II are units rich in suspension feeder organisms and detrital particles that cap unconformably the Upper Orbitolina Beds (Arnaud-Vanneau, 1980). These series are dated using benthic organisms and ammonites found in marly intervals intercalated within platform carbonates in outer shelf environments. Different calibration of biostratigraphic schemes led to different age models (Fig. 2); we follow ages from Arnaud-Vanneau et al. (2021) because our study focuses on locations previously studied by Arnaud-Vanneau (1980). The lower Urgonian Limestone Formation is dated to the late Barremian-earliest Aptian, while the Lower Orbitolina Beds, upper Urgonian Limestone Formation, and Upper Orbitolina Beds belong to the early Aptian (Arnaud-Vanneau et al., 2021). The Lumachelle I is dated close to the early-late Aptian boundary and the Lumachelle II belongs to the late Aptian (Arnaud-Vanneau and Arnaud, 1990; Hfaiedh et al., 2013).

Based on field and petrographic data Arnaud-Vanneau and Arnaud (1990) interpreted karstified or winnowed surfaces as sequence boundaries (Sbs), while facies representing the deepest depositional environment indicate maximum flooding surfaces (mfss). Aptian Sbs and mfss are labeled Ap1 to Ap5 (Fig. 2). The Urgonian Limestone started at the mfsBa3 and lasted until the SbAp2, with the Lower Orbitolina Beds being interpreted as the transgressive systems tract of the sequence Ap1. The Upper Orbitolina Beds were deposited between the SbAp2 and the SbAp3 (Arnaud-Vanneau et al., 2021). A spectacular expression of Sbs corresponds to incised valleys that cut into the Upper Urgonian Limestone, and that are filled with material from the Upper Orbitolina



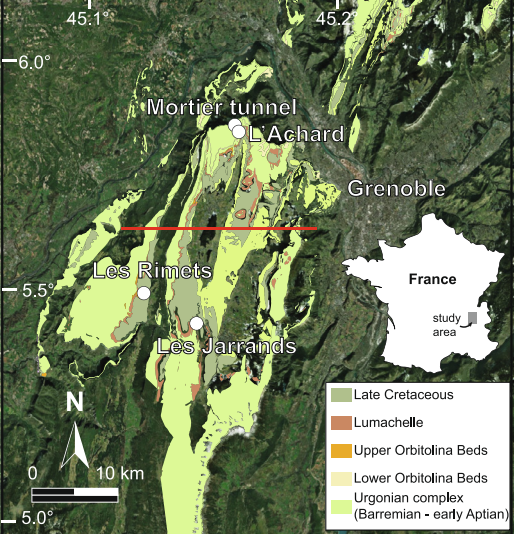
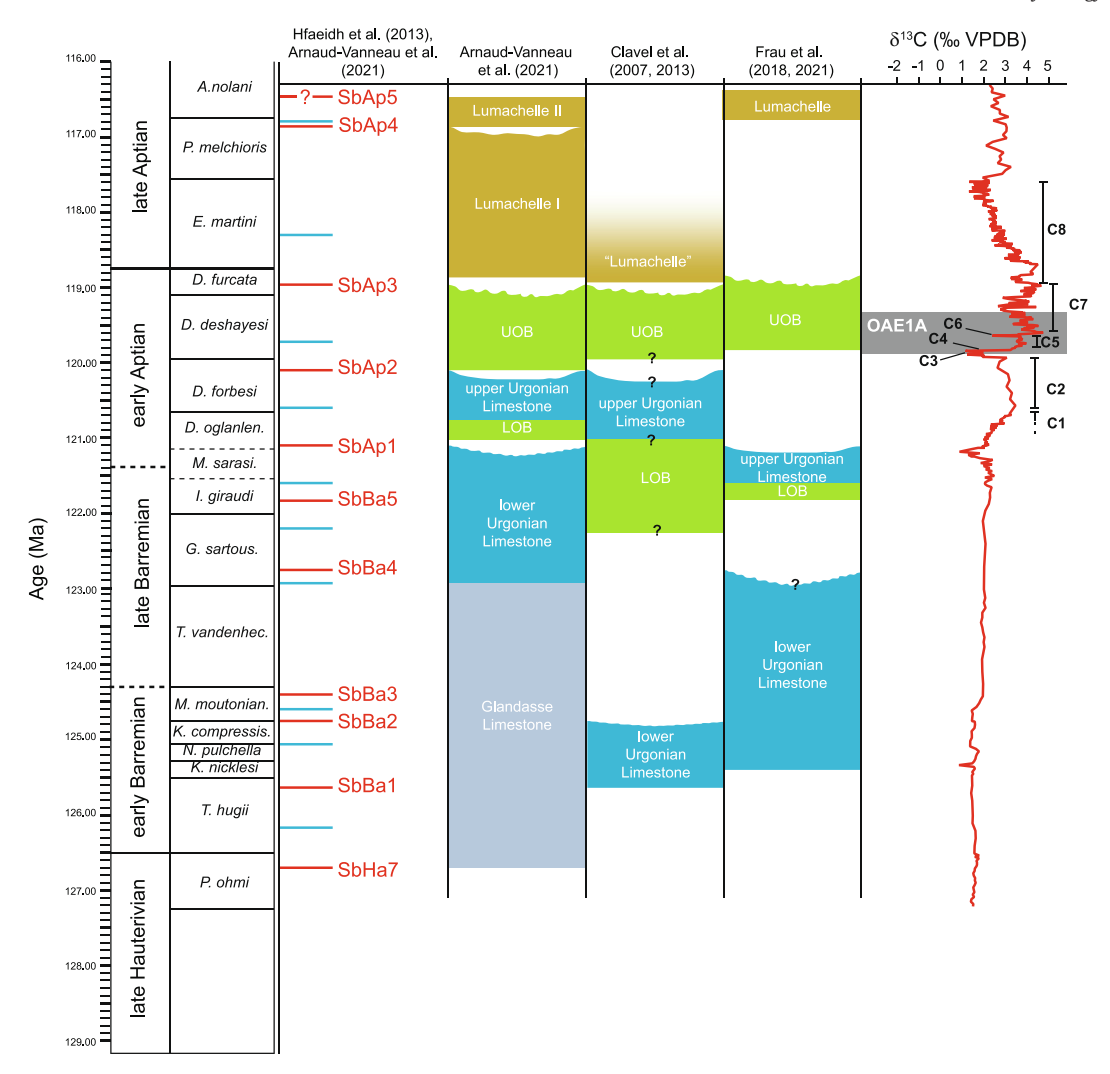


Fig. 1. Location of the study area on a paleogeographic map of the western Tethys ocean during the Aptian (redrawn from Masse et al., 1993), and of the study locations in southern France (L'Achard: 45.233392°N, 5.587566°E; Les Rimets: 45.108628°N, 5.455335°E; Mortier Tunnel: 45.238292°N, 5.582625°E; Les Jarrands: 45.084895°N, 5.520724°E). Geological map is simplified from BRGM (2024).



**Fig. 2.** Stratigraphic correlation of late Hauterivian–late Aptian formations from the Vercors region according to different authors; formations were dated based on biostratigraphic data. Absolute dating and calibration of ammonite zone are after Gradstein et al. (2020), the evolution of  $\delta^{13}$ C values is after Cramer and Jarvis (2020), and the identification of isotopic segments C1 to C8 is according to Menegatti et al. (1998). Red and blue lines on the right of ammonite zones represent sequence boundaries and maximum flooding surfaces, respectively. Abbreviations: Sb: sequence boundary; Ha: Hauterivian; Ba: Barremian; Ap: Aptian.

Beds at Les Rimets and L'Achard near the village of Autrans (Arnaud-Vanneau et al., 2005). Finally Arnaud-Vanneau et al. (2021) interpreted the depositional geometries from cliffs to demonstrate that during the late Barremian and early Aptian, the Urgonian platform prograded in the direction of the nearby Vocontian Basin located to the south and north of the Provencal platform. Combining these observations with outcrop data, these authors reported that the regional extent of the Upper Orbitolina Beds was restricted to paleovalleys and karst paleotopographies.

# 3. Material and methods

Conventional field methods were used to describe, measure, and sample four sections at a resolution of at least 50 cm. A total of 116, 21, 15, and 60 samples were obtained for the L'Achard (45.233392°N, 5.587566°E), Les Rimets (45.108628°N, 5.455335°E), Mortier Tunnel (45.238292°N, 5.582625°E), and Les Jarrands sections (45.084895°N, 5.520724°E; Fig. 1), respectively.

Only large enough samples were selected for further petrographic and geochemical analysis (n=110). They were cut using a water-cooled rock saw at the University of Texas at San Antonio (UTSA), USA. Thin sections were produced by Quality Thin Section (Tucson, Arizona, USA), slabs were prepared for microsampling for carbon and

oxygen isotope analysis, and approximately 50 g of sample was powdered using a SPEX Shatterbox 8515.

Polished thin sections were analyzed using an Olympus BX61 petrographic microscope to identify allochems and other grains present, and describe the depositional texture of each sample (Dunham, 1962). Microfacies for this region have been defined by Arnaud-Vanneau and Arnaud (1990) and Arnaud-Vanneau and Arnaud (2005). Microfacies were assigned to each sample, from the (hemi)pelagic (F0) to supratidal (F11) environment (Arnaud-Vanneau and Arnaud, 1990, 2005). Blanc-Alétru (1995) added a facies of transgression (FT) for samples with a high quartz grain content that indicates intense erosion and reworking during a rapid sea-level rise or large influx of detrital material (Fig. 3). Thin sections were digitized using an Olympus BX61 microscope at the University of Lausanne, Switzerland. Each image was loaded into JMicroVision® for point counting of 250 randomly selected grains. Sparitic cement, isopach rim, and matrix were initially counted; results were subsequently normalized to only include allochems and discard non-biogenetic components.

Slabs were microsampled at UTSA using a Voguemicro dental drill mounted on a Leica M80 stereoscope. Powdered samples were submitted to the Keck Paleoenvironmental and Environmental Stable Isotope Laboratory at the University of Kansas for oxygen and carbon isotope analyses. Approximately 70 µg of powdered sample was loaded into

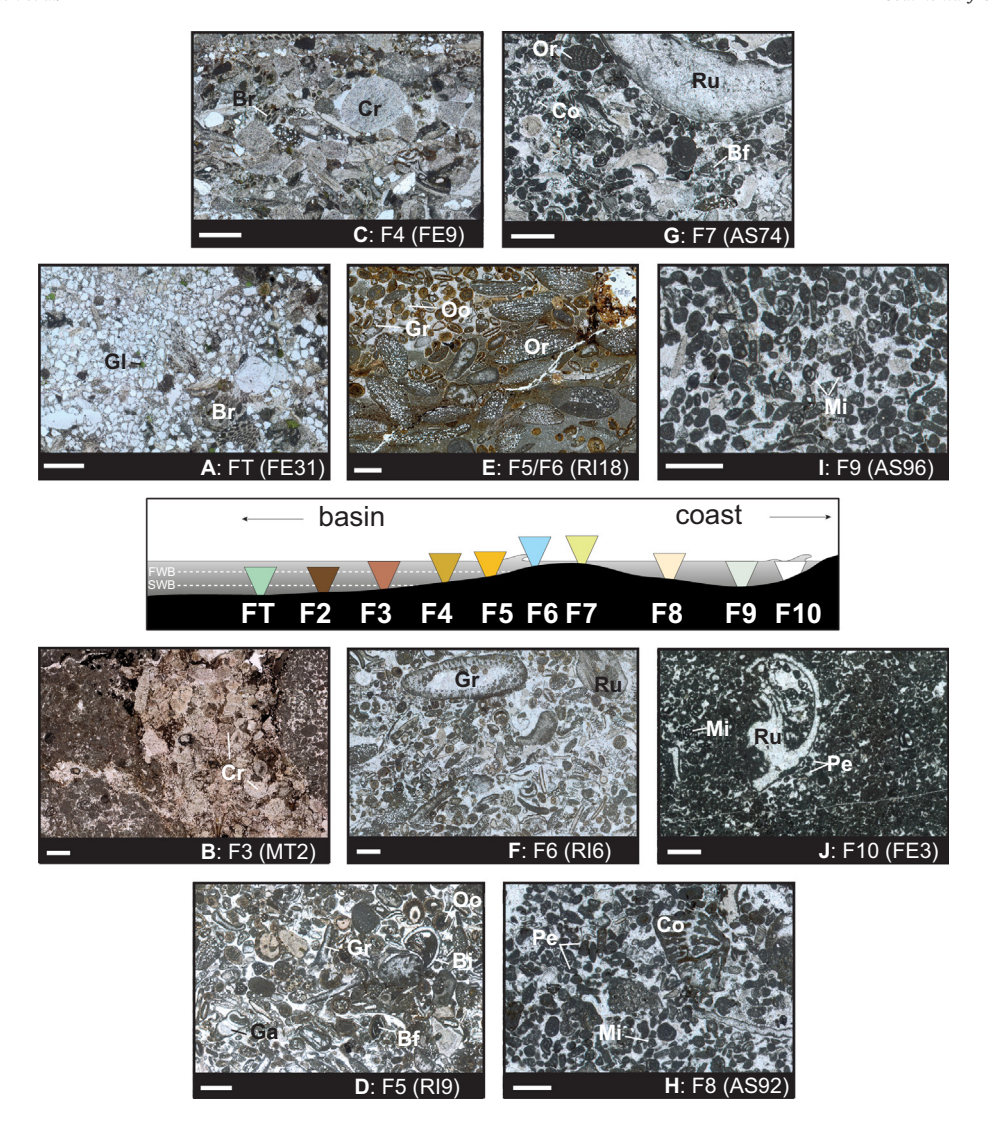


Fig. 3. Illustration and repartition of microfacies defined in thin sections, following Arnaud-Vanneau and Arnaud (2005). A: microfacies FT, quartzarenite with fragments of bryozoan (Br), crinoid, and glauconite (GI; Les Jarrands, sample FE31); B: microfacies F3, packstone with small rounded fragments of crinoid (Cr) and bryozoan (Mortier Tunnel, sample MT2); C: microfacies F4, packstone with large rounded fragments of crinoid and bryozoan (Les Jarrands, sample FE9); D: microfacies F5, packstone to grainstone with debris of green algae (Gr), bivalves (Bi), gastropods (Ga), circalittoral benthic foraminifera (Bf), and ooids (Oo; Les Rimets, sample RI9); E: microfacies F5/F6, packstone to grainstone with green algae, orbitolinid (Or) and ooid (Les Rimets, sample RI18); F: microfacies F6, grainstone with green algae, orbitolinid, and rudist fragments (Ru; Les Rimets, sample RI6); G: microfacies F7, grainstone with oral (Co), bivalve, and rudist debris, and with benthic foraminifera and orbitolinid (L'Achard, sample 74); H: microfacies F8, grainstone with pellet (Pe), green algae, miliolid (Mi), coral and bivalve fragment (L'Achard, sample AS92); I: microfacies F9, grainstone with pellet, miliolid, and bioclast (L'Achard, sample AS96); J: microfacies F10, grainstone with small pellet, miliolid, and rare rudist (Les Jarrands, sample FE3). All scale bars are 1 mm long. Abbreviations: FWB: fair-weather base; SWB: storm weather base;

vials of the Kiel IV carbonate device and reacted with >100 % phosphoric acid at 70 °C. After cryogenic purification isotopologues of  $\text{CO}_2$  were analyzed on a Thermofinnigan MAT 253 dual inlet isotope ratio mass spectrometer. The carbon and oxygen isotope ratios are reported in the delta ( $\delta$ ) notation as the per mil (%) deviation relative to the Vienna Pee Dee Belemnite standard (VPDB) using internationally calibrated standards. External reproducibility is reported as  $\pm 0.1$  % via repeated analyses of Sigma-Aldrich calcite.

Powdered samples were processed for elemental geochemical analysis at UTSA. The amount of volatile was estimated by calcination of ca. 2.0 g of powdered sample at 1050 °C in a MTI KSL-1200X muffle furnace for 90 min to calculate a loss on ignition (Dean, 1974). Glass beads were produced by mixing 9.0  $\pm$  0.001 g of lithium tetraborate (Li<sub>2</sub>B<sub>4</sub>O<sub>7</sub>) with 1.8  $\pm$  0.001 g of powdered sample into a Pt–Au crucible. Fusion at 1050 °C was performed with a Claisse© LeNeo fusion machine using a 33 minute-long automatized program. Pressed pellets were produced by homogenizing 6.65  $\pm$  0.001 g of powdered sample with 0.35  $\pm$  0.001 g of SpectroBlend® binder, and by pressing this mixture in an

aluminum cup at 5 tons for 60 s using an evacuable die set (30 mm diameter, stainless steel). Glass beads and pressed pellets were analyzed for their major and trace element concentration, respectively, using a Rigaku Primus II Wavelength Dispersive X-Ray Fluorescence spectrometer at UTSA, with a 3.6 kW beam power, and current voltage and intensity ranging between 40 and 60 kV and 60 and 90 mA, respectively, depending on the atomic number of the element targeted. The detection limit is better than 0.01 wt% and 10 ppm for major and trace elements, respectively. Standard deviation is better than 0.3 % (CaO) for major elements and varies between 0.6 (Zn) and 22.8 ppm (Ba) for trace elements, based on triplicate analysis of each sample.

From the concentration in major and trace elements,  $Zr/Zr_{sh}$  (sh = shale concentrations from Wedepohl, 1991),  $P_2O_{5xs}$ ,  $%_{terrigenous}$ ,  $Mn^*$ , and CIA (Chemical Index of Alteration) geochemical proxies were calculated (see Godet et al., 2023, and references therein). The proxy  $P_2O_{5xs}$  is calculated as an enrichment factor corrected for detrital input, and thus better identifies stratigraphic intervals with enrichment in phosphorus, while %terrigenous is a normalization of the Ti concentration in the

sample to that in the average shale of Wedepohl (1991), expressed in percent (Engelke et al., 2018, and references therein). Mn\* compares the Mn and the Fe concentration in the sample and in the average shale to evaluate the redox conditions at time of deposition (Bellanca et al., 1996). The CIA proxy relies on the leaching of calcium, sodium, and potassium during weathering of feldspars (Nesbitt and Young, 1982). Because most studied lithologies are carbonate rocks where CaO is produced in-situ, the CaO concentration is replaced by the Na<sub>2</sub>O concentration in the calculation of the CIA (McLennan, 1993).

Principal component analysis (PCA) for geochemical and point counting data was completed with an R code that uses corrplot, ggplot2 and ggfortify packages. The PCA plot of point counting data permitted identifying clusters that correspond to ecological associations. In Microsoft Excel, a pivot table helped quantify the amount of each ecological association in each sequence stratigraphic system track. To quantify the degree of ecological diversity in each sample, Hill numbers D were calculated using frequency of allochems from point counting data and a diversity index of 0.5 ( $^{0.5}$ D) and 2 ( $^{2}$ D) to favor rare and most common species, respectively (Daly et al., 2018).

# 4. Results and interpretation

4.1. Facies, depositional environments, and sequence stratigraphy

#### 4.1.1. L'Achard

The section (Fig. 4) starts with a soft bed of the Lower Orbitolina Beds with abundant large orbitolinids, fine grained bioclastic fragments, some iron coating (<5 % of allochems), and texture ranging from wackestone to packstone (microfacies F8 indicative of a lagoon environment; Table 1).

The Upper Urgonian Limestone (1 to 15 m) consists of massive gray to tan beds of medium- to coarse-grained packstone to grainstone with abundant miliolids, rudist bivalve fragments, crinoids, lithoclasts, occasional corals, green algae, and orbitolinids; this assemblage is interpreted as microfacies F5 to F7 deposited in an outer platform, subtidal to patch reef environment, following Arnaud-Vanneau and Arnaud (1990). A sequence boundary is interpreted at a switch from F8 to F6 microfacies at 15 m; it corresponds to the SbAp2 according to Arnaud (2005a).

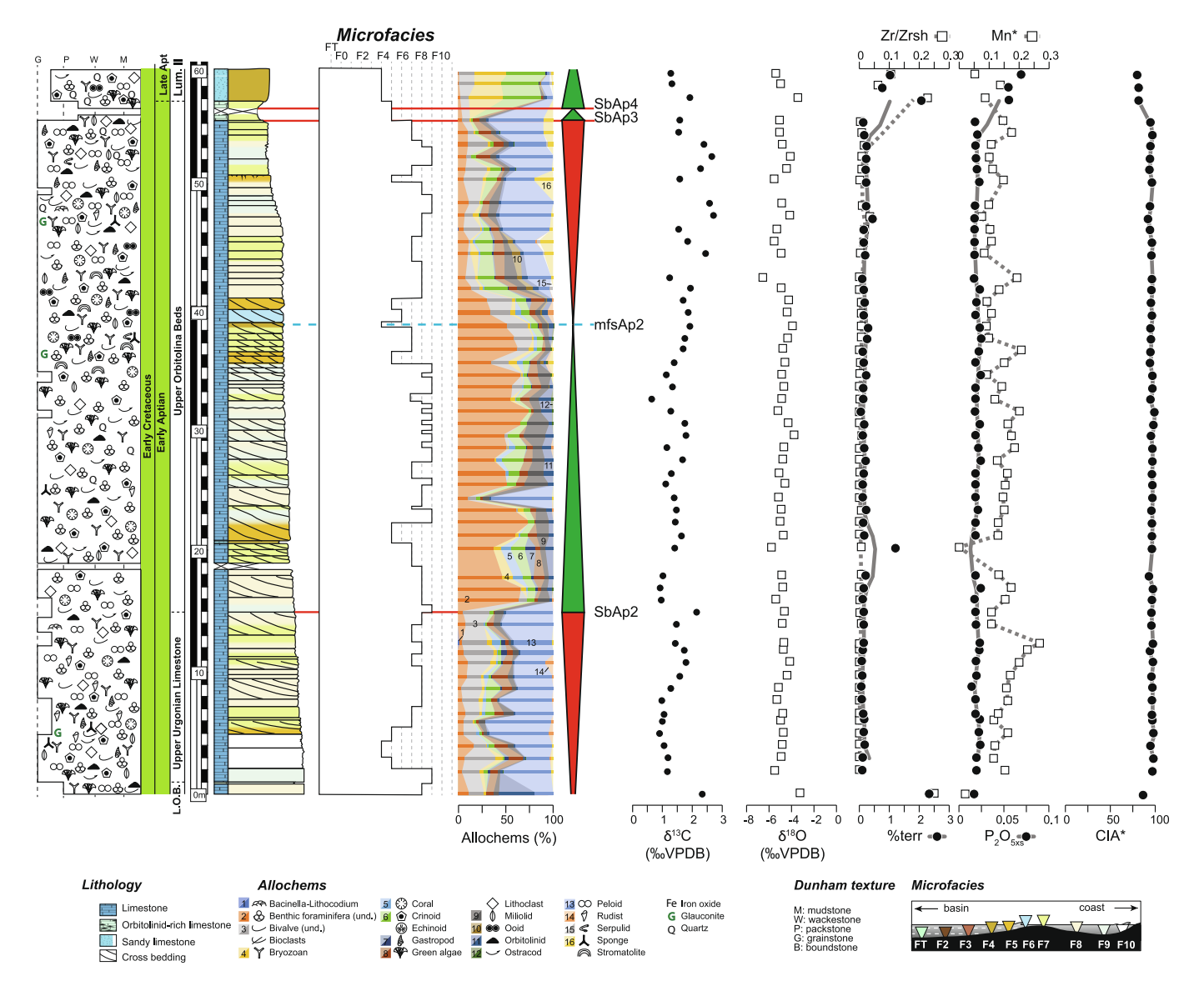


Fig. 4. Lithological column of the L'Achard Sud section, where beds are color-coded as a function of their microfacies inferred from the petrographic analysis of thin sections. This permits identifying sequence boundary (Sb) and maximum flooding surface (mfs) with red and blue lines, respectively. On the right-hand side of the lithocolumn carbon isotope ( $\delta^{13}$ C), oxygen isotope ( $\delta^{18}$ O), detrital input ( $Zr/Zr_{sh}$ , %<sub>terrigenous</sub>), redox (Mn\*), nutrient input ( $P_2O_{5xs}$ ), and continental weathering (CIA\*) values are plotted as a function of sample position in the measured section.

**Table 1**Summary of the characteristics of microfacies defined in Arnaud-Vanneau and Arnaud (2005). Microfacies F0 to F3 are not identified in this study.

Name	Texture	Skeletal components	Thickness	Sedimentary structure	Depositional environment
F0	Mudstone to wackestone	Radiolaria, ammonite	Decimetric to metric	Alternation of marlstone and limestone beds	Basin, below storm-weather wave base
F1	Wackestone	Sponge spicules	Decimetric to metric	Alternation of marlstone and limestone beds	Hemipelagic basin, below storm-weather wave base
F2	Wackestone	Sea urchins, peloid	Decimetric to metric	Wavy bedding surface	Outer shelf and slope, below storm-weather wave base
F3	Packstone to grainstone	Echinoderm, small benthic foraminifera	Decimetric	Wavy bedding surface	Outer shelf, straddling the storm-weather wave base and under the photic zone
F4	Packstone to grainstone	Bryozoan, crinoid	Decimetric to metric	Cross beddings (rare)	Outer shelf, straddling the storm-weather wave base and under the photic zone
F5	Grainstone	Large rounded bioclast of algae, large benthic foraminifera, and coral debris	Decimetric	Cross stratifications	Forereef or backreef above the fair-weather wave base
F6	Grainstone	Ooid	Decimetric	Cross stratifications	Forereef or backreef above the fair-weather wave base
F7	Grainstone	Coral	Decimetric	Oblique cross stratifications	Reef
F8	Wackestone to packstone	Large benthic foraminifera, algae, rudist and coral fragments, rare echinoderm debris	Decimetric to metric	Massive	Lagoon toward the backreef
F9	Wackestone to packstone	Small rudists, abundant miliolids	Metric	Massive	Shallow lagoon
F10	Packstone to grainstone	Micritized grains, oncoids	Metric	Massive	Innermost part of the lagoon
F11	Mudstone or grainstone	Stromatolites, rare small miliolids	Decimetric to metric	Keystone vugs, bird's eyes	Intertidal environment
F11	Packstone to grainstone	Crinoid, bryozoan	Decimetric to metric	Oblique cross stratifications	Varying environments during a transgressive phase, above the storm-weather wave base

The Upper Orbitolina Beds (15 to 57.8 m) consist of mostly grainstone with abundant miliolids, rudist bivalves, crinoids, orbitolinids, corals (up to 10 mm), green algae, occasional gastropods, bryozoans, and ooids. Microfacies vary: miliolid- and rudist-rich microfacies

F7 (moderate to high energy, subtidal to tidal environment) and F9 (shallow tidal environment of the inner platform; 13.5 to 36.3 m) transition to microfacies F5 to F7 (subtidal-tidal environment with high to moderate energy, respectively; 36.3 to 39.5 m). From 39.5 to 40 m

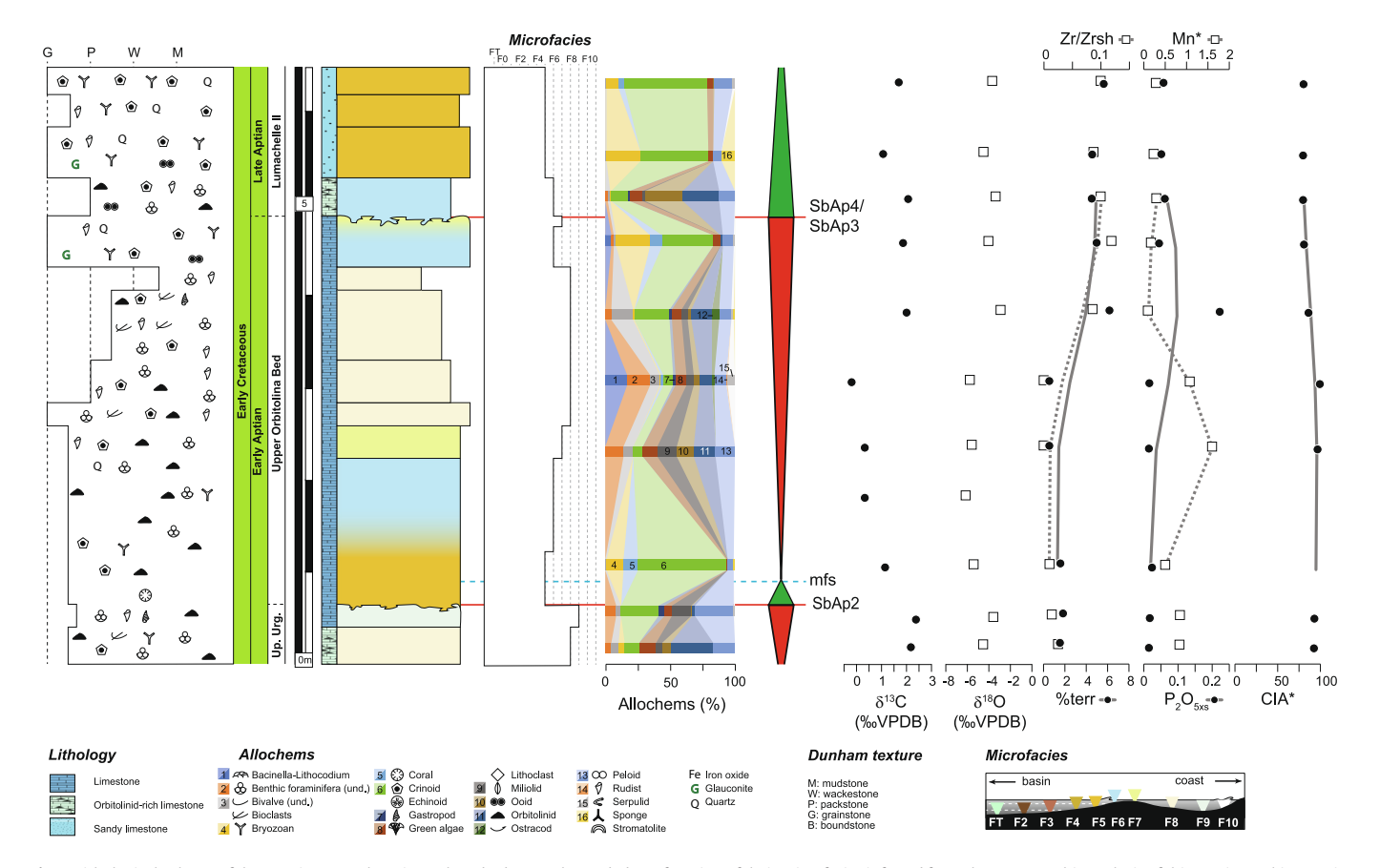


Fig. 5. Lithological column of the Mortier Tunnel section, where beds are color-coded as a function of their microfacies inferred from the petrographic analysis of thin sections. This permits identifying sequence boundary (Sb) and maximum flooding surface (mfs) with red and blue lines, respectively. On the right-hand side of the lithocolumn carbon isotope ( $\delta^{13}$ C), oxygen isotope ( $\delta^{18}$ O), detrital input (Zr/Zr<sub>sh</sub>, %<sub>terrigenous</sub>), redox (Mn\*), nutrient input (P<sub>2</sub>O<sub>5xs</sub>), and continental weathering (CIA\*) values are plotted as a function of sample position in the measured section.

microfacies F4 was deposited in a deep outer platform environment; it marks the deepest environment encountered in the section, and is interpreted as the maximum flooding surface Ap2 of Arnaud (2005a). From 40 to 50.8 m microfacies in the Upper Orbitolina Beds range from F8 to F5 from the base to the top of the interval; this indicates a deepening-upward trend from a lagoonal to outer platform subtidal environment, whereas microfacies F7 to F9 from 50.8 to 55.2 m (patch reef to inner platform environment, respectively) are interpreted as a shallowing-upward trend. From 55.2 to 57.8 m orbitolinid-rich microfacies F5 indicates a forereef or backreef environment above the fair-weather wave base.

The Lumachelle II (57.8 to 60.3 m) is a tan to light brown, massively bedded sandy beds of wackestone–packstone to packstone–grainstone. It contains abundant crinoids, bryozoans, bivalve fragments, varying amounts of detrital quartz grains, and occasional glauconite (microfacies F4, deep outer platform subtidal environment). The SbAp3 is placed at the transition from F7 to F5 microfacies at 55.2 m while the position of SbAp4 is inferred in a hillslope where rocks are poorly exposed between the Upper Orbitolina Beds and the Lumachelle II (Fig. 2).

# 4.1.2. Mortier Tunnel

The Upper Urgonian Limestone (0 to 0.75 m) comprises massive beds of packstone–grainstone that are fractured, gray in color (Fig. 5).

It has abundant large orbitolinids, miliolids, bioclastic fragments, occasional rudists, and green algae (microfacies F8) that indicate a lagoonal environment. The topmost sample of the Upper Urgonian Limestone includes abundant miliolids, occasional orbitolinids, and green algae (microfacies F9, inner platform setting); it is capped by a karst filled by a grainstone with crinoids, miliolids, orbitolinids, some lithoclasts and bioclastic fragments (microfacies F4, subtidal environment). The karst surface is interpreted as the SbAp2.

The Upper Orbitolina Beds (0.75 to 4.95 m) include abundant miliolids, rudists, orbitolinids, occasional ooids, green algae, and lithoclasts. Depositional textures range from mudstone–wackestone (5.2 m) to grainstone (3.6 m). The depositional environment gradually shifts from an outer platform shallow subtidal (microfacies F5, 0.75 to 1.1 m) to a forereef (microfacies F6 at 2 m), and lagoonal environment (microfacies F7 and F8 up to 4.35 m). The last bed of the Upper Orbitolina Beds (4.34 to 4.95 m) indicates a backreef (microfacies F6) to shallow lagoonal (microfacies F7) environment based on the presence of large orbitolinids and ooids. The mfsAp2 is interpreted in microfacies F5 at 0.9 m.

The Lumachelle II (4.95 to 6.5 m) is tan to light brown and is more prone to erosion than underlying formations. Its facies corresponds to an orbitolinid- and ooid-rich packstone to grainstone with abundant bryozoans and crinoids, and occasional quartz and glauconite

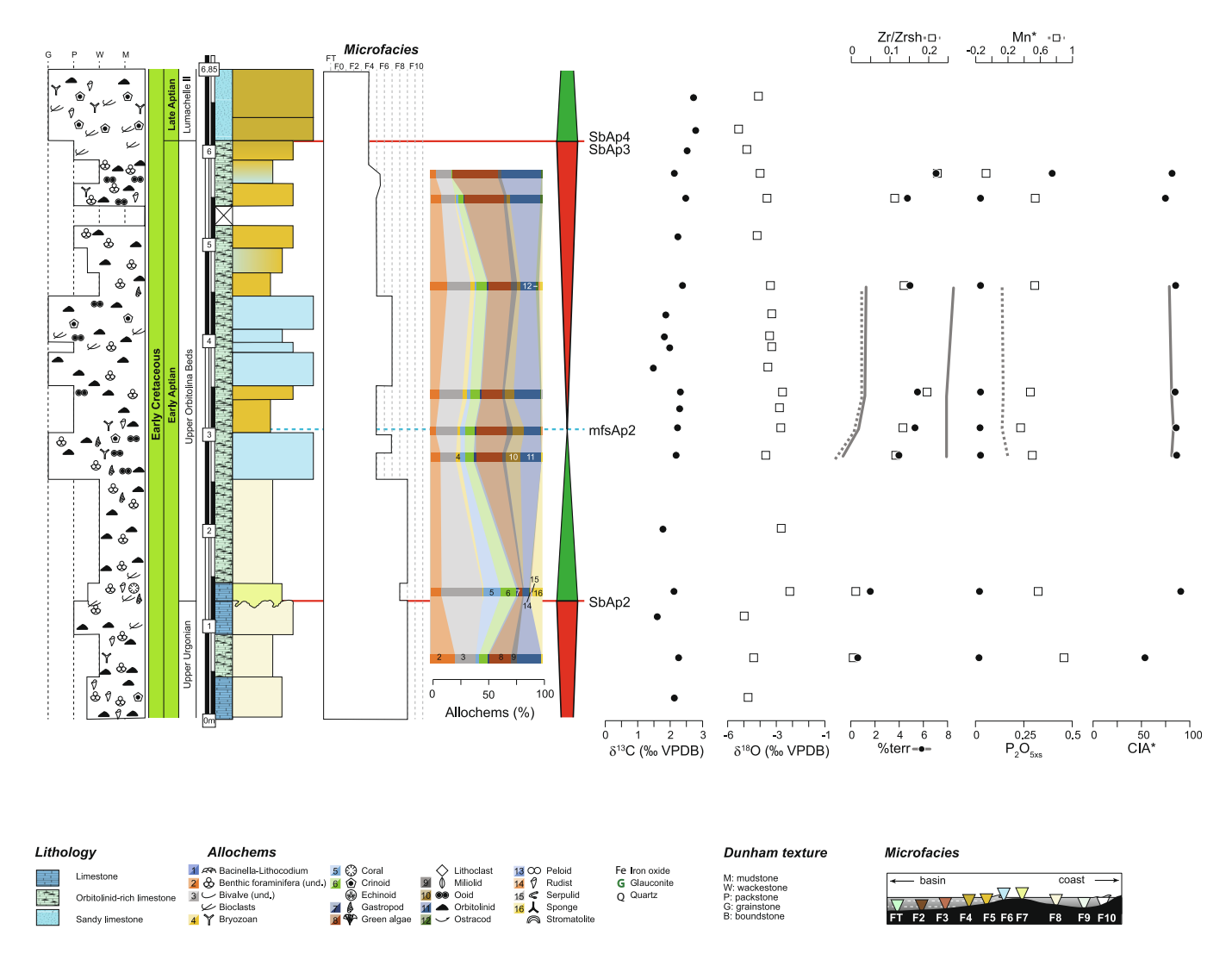


Fig. 6. Lithological column of the Les Rimets section, where beds are color-coded as a function of their microfacies inferred from the petrographic analysis of thin sections. This permits identifying sequence boundary (Sb) and maximum flooding surface (mfs) with red and blue lines, respectively. On the right-hand side of the lithocolumn carbon isotope ( $\delta^{13}$ C), oxygen isotope ( $\delta^{18}$ O), detrital input (Zr/Zr<sub>sh</sub>, %<sub>terrigenous</sub>), redox (Mn\*), nutrient input (P<sub>2</sub>O<sub>5xs</sub>), and continental weathering (CIA\*) values are plotted as a function of sample position in the measured section.

(microfacies F5, outer platform subtidal environment). The contact between the Upper Orbitolina Beds and the Lumachelle II corresponds to a karst surface at 4.95 m, is associated with an abrupt fauna change, and corresponds to stacked SbAp3 and SbAp4 as the Lumachelle I is missing.

# 4.1.3. Les Rimets

The Les Rimets outcrop (Fig. 6) features an incised valley into the Upper Urgonian Limestone, filled with deposits of the Upper Orbitolina Beds, and capped by the Lumachelle II (Arnaud-Vanneau and Arnaud, 1990). The Upper Urgonian Limestone (0 to 1.25 m) is a white to light gray packstone rich in miliolids and orbitolinids with bioclastic fragments, rudists, and miliolids, which is interpreted as a lagoonal (microfacies F8) to an inner platform subtidal (microfacies F9) environment. Its top surface is karstified and is interpreted as the SbAp2.

The Upper Orbitolina Beds are medium to dark gray in color and are organized in thin beds of variable competency. From 1.25 to 2.5 m a marly wackestone with corals, bioclastic fragments, occasional orbitolinids, and bivalve fragments is interpreted as being deposited in a backreef (microfacies F8, 1.25 to 1.45 m) to a shallow lagoonal environment (microfacies F9, 1.45 to 2.5 m). From 2.5 to 3 m the facies transitions into an orbitolinid- and ooid-rich packstone to grainstone with green algae, bivalves, miliolids, crinoids, and well-rounded grains

(microfacies F6). At 3 m the facies changes to an orbitolinid- and ooid-rich packstone with noticeable thin cross-stratifications (microfacies F5); we interpret the mfsAp2 in this interval because the overlying facies (3.5 to 4.6 m) transitions to microfacies F6 (orbitolinid and ooid grainstone with higher quantities of bivalve fragments, bryozoans, miliolids, and rounded bioclastic fragments) indicative of shallower environments. The remainder of the Upper Orbitolina Beds (4.6 to ca. 6 m) correspond to orbitolinid- and ooid-rich wackestone to packstone with fewer bivalve, bryozoan, and crinoid allochems, indicative of an outer platform shallow subtidal (microfacies F5) to an outer platform tidal (microfacies F6) environment.

The Lumachelle II (6 to 6.85 m) consists of tan to light brown, coarse grainstone with abundant quartz, crinoid and bryozoan (microfacies F4, outer platform, deep subtidal environment). The boundary between the Upper Orbitolina Beds and the Lumachelle II is interpreted as the stacked SbAp3–SbAp4.

# 4.1.4. Les Jarrands

At the base of the outcrop, the Upper Orbitolina Beds (0 to 2.1 m; Fig. 7) include beds of gray, fine-grained miliolid packstone to grainstone with occasional orbitolinid, oncoid, lithoclast, and large rudist. The occurrence of *Bacinella–Lithocodium*, lithoclasts, miliolids, orbitolinids, bird's eyes, and coated rudist fragments indicates microfacies F9 (inner platform shallow tidal environment) to F10

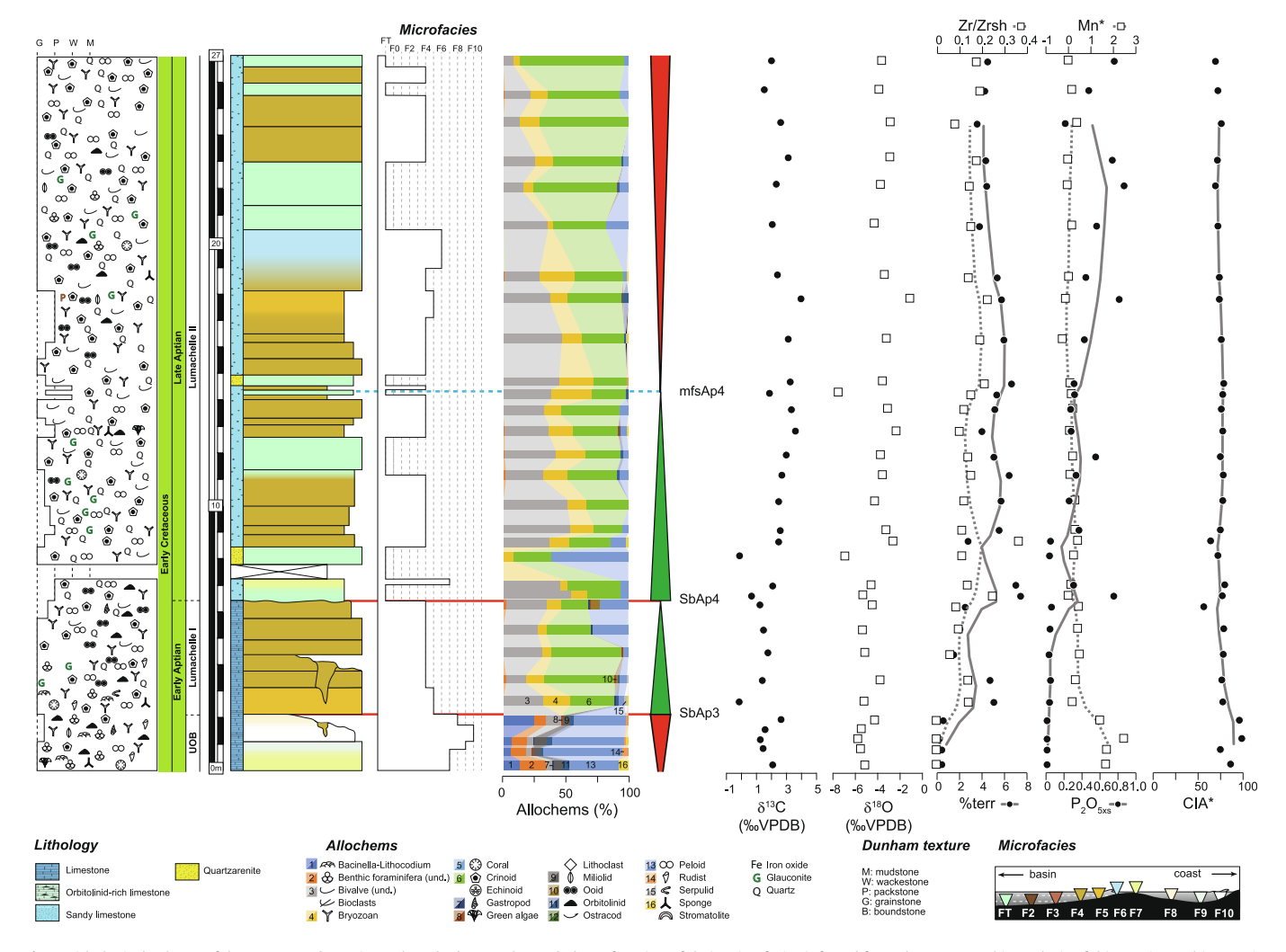


Fig. 7. Lithological column of the Les Jarrands section, where beds are color-coded as a function of their microfacies inferred from the petrographic analysis of thin sections. This permits identifying sequence boundary (Sb) and maximum flooding surface (mfs) with red and blue lines, respectively. On the right-hand side of the lithocolumn carbon isotope ( $\delta^{13}$ C), oxygen isotope ( $\delta^{18}$ O), detrital input ( $Zr/Zr_{sh}$ , %<sub>terrigenous</sub>), redox (Mn\*), nutrient input ( $P_2O_{5xs}$ ), and continental weathering (CIA\*) values are plotted as a function of sample position in the measured section.

(supratidal environment). The morphology of *Bacinella–Lithocodium* falls into the patchy–cloudy (samples FE-1 and 2) and lump (samples FE-3 and 5) categories of Rameil et al. (2010), confirming their deposition in a shallow subtidal environment with high sedimentation rate and oxygen level, and low nutrient input and alkalinity. At the top of the Upper Orbitolina Beds, an irregular surface infilled by facies from the Lumachelle I corresponds to the SbAp3.

Beds of the Lumachelle I (2.1 to 6.4 m) are light tan, often laterally truncated, display cross-stratification, and have a coarse-grained texture. The lowermost beds (2.1 to 4.4 m) correspond to a coarse-grained crinoid and bryozoan grainstone with occasional orbitolinids, bivalves, and quartz. Top beds (4.4 to 6.4 m) are medium-grained crinoid and bryozoan grainstone with more ooids and less quartz, glauconite, rudist, and orbitolinid than in the lower beds. Beds of the Lumachelle I are interpreted to be deposited in an outer platform, shallow subtidal (microfacies F5) to deep subtidal (microfacies F4) environment. The Lumachelle I ends with an irregular surface interpreted as the SbAp4.

The Lumachelle II (6.4 to 27 m) is tan to light brown in outcrop and is more prone to erosion than underlying formations. The lowermost samples (6.4 to 8.5 m) correspond to a quartz-rich (30–75 %) grainstone to calcareous quartzarenite with crinoid, bryozoan, rudist, and occasional glauconite; the lack of orbitolinid and ooid distinguishes this formation from the Lumachelle I. The interval between 8.5 and 14 m corresponds to intermittent marls with less quartz. The depositional texture ranges from packstone to grainstone with crinoid, bryozoan, large rudist, quartz (8-25 %), and occasional glauconite. A calcareous quartzarenite (70 % quartz) interval (14 to 14.15 m) overlies a thin, intermittent marl zone, and includes crinoid, bryozoan, and rudist fragments. From 14.5 to ca. 18 m a marly interval with less quartz (5-30 %) mimics the interval between 8.5 and 14 m. The uppermost Lumachelle II (18 to 27 m) is a clean, coarse-grained crinoid- and bryozoan-rich grainstone with intervals rich in quartz (10-40 %), occasional bivalves and glauconite. Facies in the Lumachelle II indicate an outer platform subtidal environment (microfacies F4) intercalated with facies of transgression (FT). The mfsAp4 is interpreted in a marly interval at 14.5 m.

# 4.1.5. Point-counting data

Point counting data are plotted alongside lithological columns in Figs. 4 to 7; mean values in each lithostratigraphic unit are summarized in Table 2.

The only sample from the Lower Orbitolina Beds indicates the dominance of orbitolinids (mean of 37 %; Table 2) and bivalves (mean of 16 %). In the Upper Urgonian Limestone the most abundant allochem is pellet (mean of 34 %) followed by bivalve (15 %) and lithoclast (mean of 11 %). The Upper Orbitolina Beds are dominated by benthic foraminifera (mean of 26 %) and pellet (mean of 15 %); on average the orbitolinid represents 6 % of allochems. The Lumachelle I is dominated by crinoid (mean of 34 %) and bryozoan (mean of 23 %), while quartz (mean of 30 %) and crinoid (mean of 28 %) are the most occurring grains in the Lumachelle II.

# 4.2. Stable carbon and oxygen isotopes

At the L'Achard section  $\delta^{13}C$  values remain around 1.1 % from 2.1 to 7.8 m before they increase by ca. 0.45 % from 9.9 to 31.7 m. A small negative spike (amplitude of ca. -0.4 %) from 32.7 to 35.7 m precedes an increase of 1.2 % up to 53 m before  $\delta^{13}C$  values decrease back through the rest of the section (Fig. 4).  $\delta^{18}O$  values increase from 2.1 to 38.7 m (amplitude of +0.5 %), then decrease to a minimum of -6.4 % at 42.8 m before a second increasing-upward trend to the top of the section. A cross plot of  $\delta^{13}C$  vs.  $\delta^{18}O$  values reveals a poor correlation ( $R^2=0.2$ ) for the whole section (Fig. 8).

At Mortier Tunnel (Fig. 5) a negative excursion in  $\delta^{13}$ C values from 1.8 to 3.1 m (amplitude of -1.8 ‰) is followed by an increase up to

Occurrence of allochems and detrital grains (mean values in percent) in each formation consi

direire	e or amornic	divine of anotherns and decream plants (mean value) in each formation compared as	anis (incan vara	com percent	in cacii	10 marion	constant ca.												
	Bacinella	Bacinella Benthic foram. Bivalve und. Bryozoan Coral Crinoid	Bivalve und.	Bryozoan	Coral	Crinoid	Gastropod	Glauconite	Green algae	Miliolid	Ooid	Orbitolinid	Ostracod	Pellet	Quartz	Quartz	Serpulid	Sponge	Stromatolite
OB	0	11	16	2	0	0	0	0	8	9	0	37	0	19	0	0	0	0	0
pUrg	$\nabla$	7	18	3	2	7	2	$\nabla$	6	2	$\nabla$	4	$\overline{\lor}$	38	~	1	$\stackrel{\vee}{\sim}$	~	3
08	1	26	10	3	2	10	1	<u>^</u>	8	7	2	7	\ \	16	1	$\nabla$	$\nabla$	2	1
UM1	0	1	28	8	0	35	√	1	1	0	2	0	0	17	7	0	0	0	0
IM2	0	<u></u>	18	12	<u></u>	29	<u></u>	2	_	7	_	,	0	Δ	30	7	7	7	_

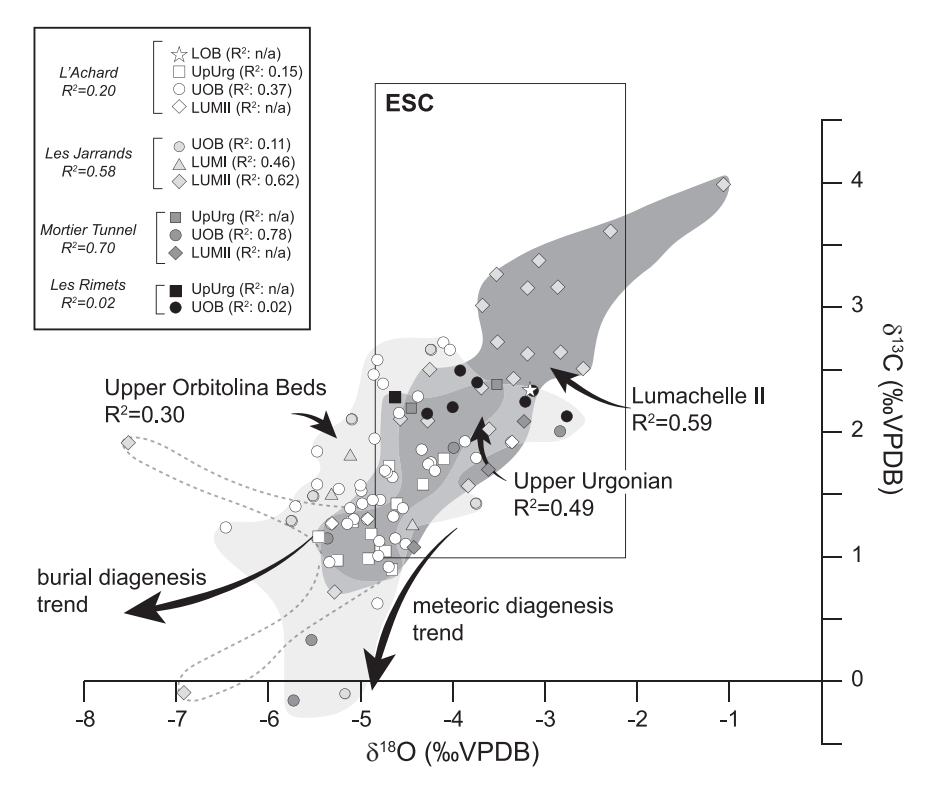


Fig. 8. Cross-plot of  $\delta^{13}$ C vs.  $\delta^{18}$ O values color coded for samples from the Vercors region. Pearson coefficients of correlation ( $R^2$ ) are calculated for each formation at each location (results in the legend) and for each formation for the whole study are (results in the plotting area).  $R^2$  values are not calculated for small (<3 observations) datasets. Estimated Seawater Calcite (ESC) values are from Herrle et al. (2004, and references therein).

1.7 % at the top of the outcrop. Trends in  $\delta^{18}$ O values are nearly identical to the  $\delta^{13}$ C trends: a decreasing trend to a minimum of -6.1 % (1.8 to 3.1 m) precedes an increase in values (amplitude of +2 %) from 3.1 m to the top of the section. A cross-plot of  $\delta^{13}$ C vs.  $\delta^{18}$ O values (Fig. 8) indicates a moderately strong correlation ( $R^2 = 0.7$ ).

At Les Rimets (Fig. 6)  $\delta^{13}$ C values increase by ca. 0.5 % from the base to the top of the measured section with negative excursions of an amplitude of ca. 0.5 % at 1.1 and 4.7 m. The evolution of  $\delta^{18}$ O values is characterized by low values (minimum of -5.1 % at 1.1 m) before a maximum of -2.8 % is reached at 1.3 m. The remainder of the section corresponds to a steady trend toward more negative values. A cross plot of  $\delta^{13}$ C vs.  $\delta^{18}$ O values reveals a poor correlation ( $R^2 = 0.02$ ).

At Les Jarrands (Fig. 7)  $\delta^{13}$ C values decrease from 0.2 to 6.6 m (amplitude of -1.35 %), increase up to 17.7 m (amplitude of 2.1 %), and decrease through the remainder of the section (amplitude of 1.2 %).  $\delta^{18}$ O values trend positively from 0.2 to 3.4 m (0.8 % amplitude), negatively from 4.0 to 6.6 m (0.65 % amplitude), and positively up to the top of the section (2.65 % amplitude). A cross plot between  $\delta^{13}$ C and  $\delta^{18}$ O values indicates a fair correlation ( $R^2 = 0.58$ ; Fig. 8).

The cross plot of  $\delta^{13}$ C vs.  $\delta^{18}$ O values (whole dataset) shows a systematic deviation from the Estimated Seawater Composition (ESC) toward lower  $\delta^{13}$ C and more negative  $\delta^{18}$ O values (Fig. 8), with two Upper Orbitolina Beds and one Lumachelle II samples having negative  $\delta^{13}$ C values.

# 4.3. Elemental geochemistry

At L'Achard Zr/Zr<sub>sh</sub> values remain lower than 0.01 except in the Lower Orbitolina Beds (base of the section) and in the Lumachelle II (57.6 to 59.6 m) where maximum values of 0.25 and 0.23 are reached, respectively (Fig. 4). Aside from a high value of 6.1 % at 20.5 m, %<sub>terr</sub> values follow a similar trend with a maximum value in the Lumachelle II (10.4 % at 57.6 m).  $P_2O_{5xs}$  values average at 0.02 from the base of the section to the base of the Lumachelle II at 57.6 m high, then increase

up to a maximum of 0.07 at the top of the section. A large scattering is observed in Mn\* values that range from 0 to 1.1 throughout the section with no apparent trend. CIA\* values do not vary much from the base of the section to 57.6 m with an average of 96 % in this interval, while values in the Lumachelle II decrease down to 80.5 %.

At Mortier Tunnel Zr/Zr<sub>sh</sub> and  $%_{terr}$  values remain lower than 0.05 and 2 %, respectively, from 0 to 3 m; values increase up to 0.12 and ca. 6 % at 3.8 m. Zr/Zr<sub>sh</sub> and  $%_{terr}$  values slightly decrease in the Lumachelle II (0.09 and 4.5 %, respectively), before reaching values of 0.1 and 5.6 %, respectively toward the top of the section.  $P_2O_{5xs}$  values average at ca. 0.02 from the base of the section up to 3.1 m, then increase up to 0.225 at 3.8 m. In the remainder of the section  $P_2O_{5xs}$  values average at 0.06. Mn\* values average around 0.7 from the base of the section up to 1.1 m before they increase to a maximum of 1.6 at 2.3 m. Mn\* values then decrease down to ca. 0.2 at 4 m and remain low up to the top of the section. CIA\* values slightly decrease upward, from 93.1 % at the base of the section up to 80.8 % at its top.

At Les Rimets Zr/Zr $_{\rm sh}$  and  $\%_{\rm terr}$  values display identical increasing-upward trends, from 0.01 and 0.6 % at the base of the section up to 0.225 and 7.1 % at its top, respectively (Fig. 6).  $P_2O_{5xs}$  values average at ca. 0.2 throughout the section except a high value of 0.4 at 5.8 m. Mn\* values average at ca. 0.6 throughout the section except a low value of -0.1 at 5.8 m. CIA\* values increase from 55 to 92.8 % from 0.7 to 1.3 m, and subsequently average around 85 % in the remainder of the section.

At Les Jarrands Zr/Zr<sub>sh</sub> and  $\%_{terr}$  values display an increasing-upward trend from 0 and 0.5 % at the base of the section to 0.36 (at 8.6 m) and 7.5 % (at 6.6 m), respectively.  $\%_{terr}$  values then remain at ca. 6 % from 6.6 to 14.2 m, while Zr/Zr<sub>sh</sub> values rapidly decrease from a maximum value of 0.36 at 8.6 m down to 0.1 at 12.7 m, before increasing back to 0.22 at 17.7 m. Both Zr/Zr<sub>sh</sub> and  $\%_{terr}$  values display decreasing-upward trends in the remainder of the section to reach values of 0.175 and 4.6 % at the top of the section, respectively.  $P_2O_{5xs}$  values are the lowest in the Upper Orbitolina Beds (average value of 0.03). They

increase in the Lumachelle I and in the Lumachelle II up to 14.5 m with maximum values of 0.76, 0.82, and 0.87 at 6.6, 17.7, and 22.0 m, respectively. CIA\* values decrease upward throughout the section, from 87% at its base up to 69.8% at its top.

# 4.4. Data analysis

In the PCA plot of geochemical data (Fig. 9) Lower Orbitolina Beds, some Upper Orbitolina Beds, and Lumachelle II datapoints align with vectors for detrital (e.g.,  $Zr/Zr_{sh}$ ,  $%_{terr}$ ) and nutrient supply ( $P_2O_{5xs}$ ) in the right-hand side quadrant. On the left-hand side quadrant, Upper Urgonian Limestone and most Upper Orbitolina Beds datapoints align with CaO, CIA\*, and Mn\* vectors. In the upper, middle part of the plot, the vector for SiO<sub>2</sub> aligns with Lumachelle I, some Upper Orbitolina Beds and some Lumachelle II datapoints. The score of PC1 and PC2 sums at 69.3 %; loadings of each parameter on PC1 and PC2 are reported in Fig. 9.

The PCA of point counting data defines three clusters in the top right (Tier 1: *Bacinella–Lithocodium*, gastropod, lithoclast, pellet, rudist, serpulid, and sponge), bottom right (Tier 2: undifferentiated benthic foraminifera, coral, green algae, miliolid, ooid, orbitolinid, ostracod, and stromatolite), and bottom left (Tier 3: bivalve, bryozoan, crinoid, glauconite, and quartz) of the plot. Datapoints of Upper Urgonian Limestone and ca. 30 % of Upper Orbitolina Beds fall into Tier 1, while Lower Orbitolina Beds, two Upper Urgonian Limestone and ca. 70 % of Upper Urgonian Limestone datapoints fall into Tier 2, and datapoints of Lumachelle I, Lumachelle II, and some Upper Orbitolina Beds fall into Tier 3. The score of PC1 and PC2 sums at 31.43 %; loadings of each parameter on PC1 and PC2 are reported in Fig. 9.

The proportion of each tier is plotted alongside a composite  $\delta^{13}$ C curve for the study area assembled based on the recognition of Sbs and mfss (Fig. 10). In the Upper Urgonian Limestone Tier 1, Tier 2, and Tier 3 represent 34, 45, and 21 % of ecosystems, respectively. In the Upper Orbitolina Beds Tier 1, Tier 2, and Tier 3 represent 24, 52.5, and 23.5 % of ecosystems, respectively. In the Lumachelle I and II,

Tier 1, Tier 2, and Tier 3 represent 14.5, 3.5, and 82 % of ecosystems, respectively. Regarding ecological diversity, Hills numbers that favor common species ( $^2$ D) display a slightly increasing trend from 0.5 up to 1.0 at 42.6 m, then values drop down to 0.5 in the remainder of the Upper Orbitolina Beds. In the Lumachelle I and II,  $^2$ D values increase back up to 0.9. Hills numbers that favor rare species ( $^{0.5}$ D) display more scattering in the Upper Urgonian Limestone and the Upper Orbitolina Beds, with values ranging from 3.3 (23.9 m) to 14.2 (26.6 m). In the upper part of the Upper Orbitolina Beds, a decreasing-upward trend parallels the one described in  $^2$ D values. In the Lumachelle I and II,  $^{0.5}$ D values increase up to 7.9 (56.8 m) before they decrease down to 3.8 at the top of the section; this trend is interrupted by a spike in values up to 8.7 at 62.1 m.

#### 5. Discussion

#### 5.1. Identification of the OAE1a

The OAE1a was first identified in deep marine series where high organic matter contents indicate anoxia (Schlanger and Jenkyns, 1976), and it was subsequently associated with a perturbation in the global carbon cycle reflected in the evolution of  $\delta^{13}\text{C}$  values (Weissert et al., 1979; Weissert, 1989; Menegatti et al., 1998). In shallow-marine settings, high total organic carbon content is rarely preserved because of the rapid oxidation of organic matter, but trends in  $\delta^{13}\text{C}$  values can help identify the OAE1a if isotope segments defined by Menegatti et al. (1998) are recognized in the absence of strong diagenetic alteration that could impact  $\delta^{13}\text{C}$  values (e.g., Swart, 2015).

In Vercors, because studied outcrops did not provide a thick, continuous and complete sedimentary archive representative of the latest Barremian–early Aptian, we compiled a composite  $\delta^{13}\text{C}$  curve (Fig. 10) based on the sequence stratigraphic interpretation and correlation of studied sections to help locate the record of the OAE1a within the sedimentary succession. The chemostratigraphic interpretation of the composite  $\delta^{13}\text{C}$  curve requires the evaluation of the preservation of the

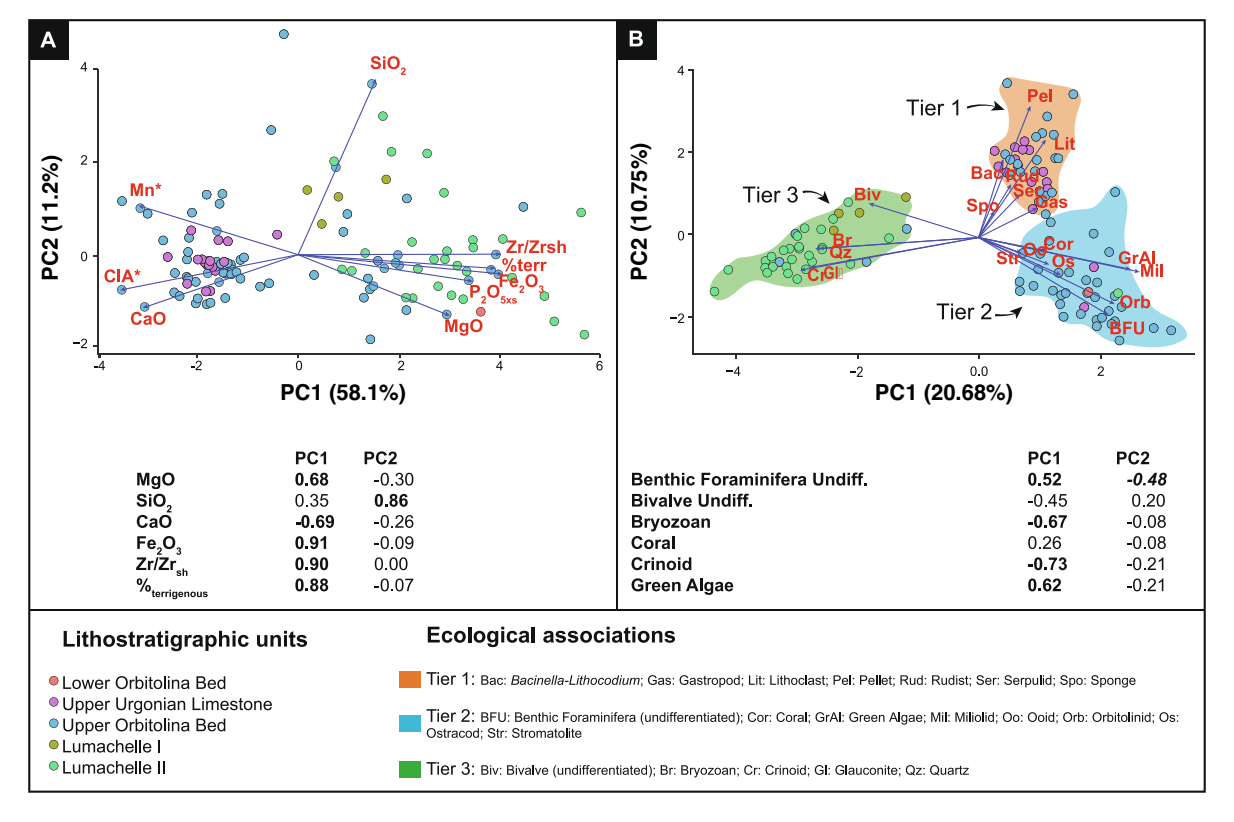


Fig. 9. Principal component analysis (PCA) plots of geochemical (A) and point counting data (B).

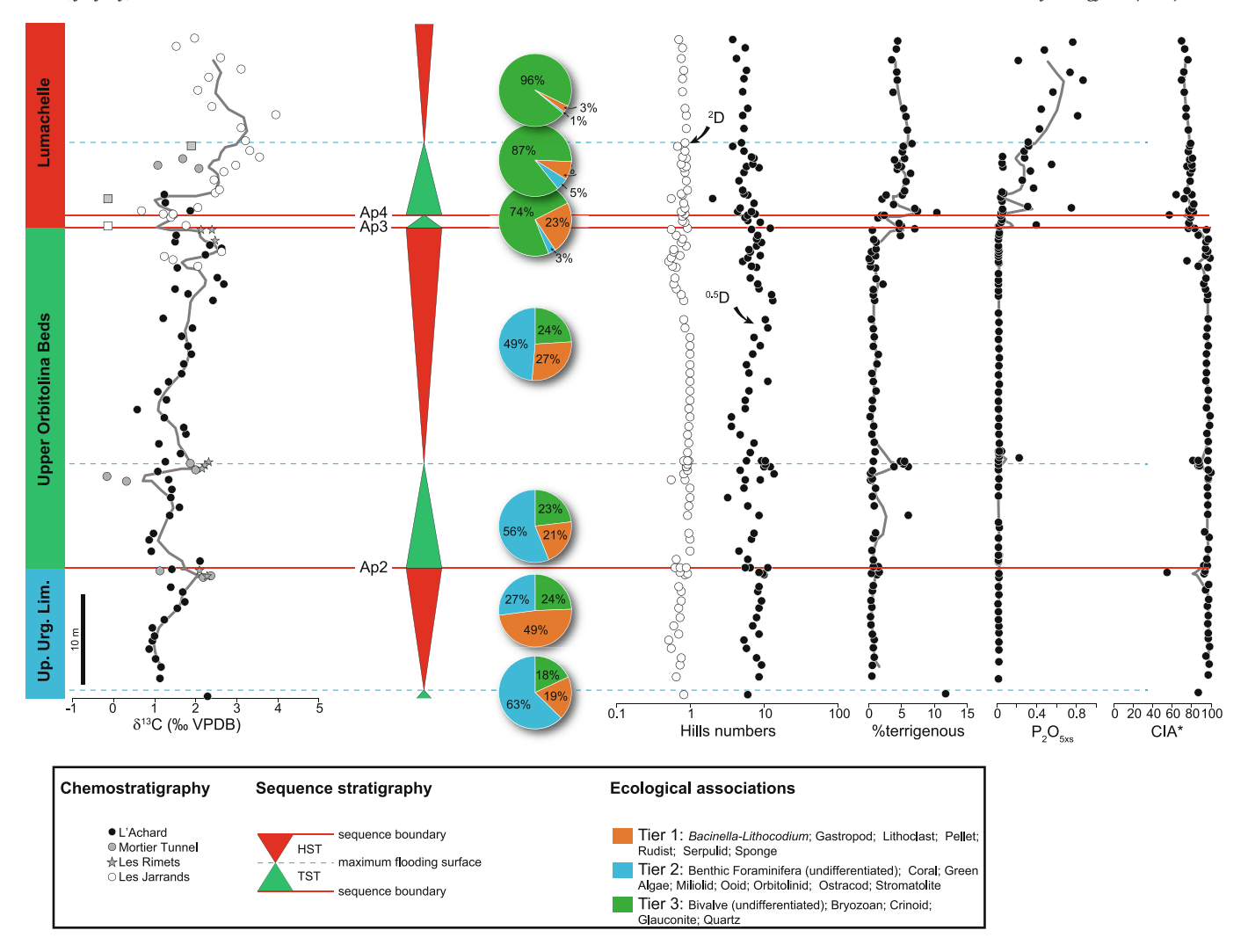


Fig. 10. Composite carbon isotope curve and sequence stratigraphic scheme (adapted from Arnaud, 2005b) for the lower to upper Aptian succession of the Vercors region. Horizontal red and blue lines represent sequence boundaries and maximum flooding surfaces, respectively. In the  $\delta^{13}$ C curve square symbols identify samples altered by meteoric (white) or burial (gray) diagenesis. The recognition of the OAE1a isotope segments (C3 to C7) is based on comparison of our data with trends in  $\delta^{13}$ C values from Menegatti et al. (1998). The lower Aptian curve from the Vocontian Basin is redrawn from Föllmi et al. (2006) and references therein, where the isotope segments of Menegatti et al. (1998) are placed. For each system tract a pie chart illustrated the proportion of each ecological association. Elemental geochemical data helped calculate proxies for major paleoenvironmental parameters; note that a major increase in  $P_2O_{5XS}$  is coeval with the increase of proportion of ecological Tier 3.

isotope signal. Carbonates formed in deeper marine settings are less susceptible to be altered by early meteoric diagenesis, and their  $\delta^{13}$ C values may reflect a rock-buffered diagenetic system (Swart, 2015). The  $\delta^{13}$ C and  $\delta^{18}$ O values for Lower Cretaceous (hemi-)pelagic carbonates from the Vocontian Basin (southeastern France) range between 0.98 and 4.76 %, and -2.11 and -4.81 %, respectively (Herrle et al., 2004); any departure from these ranges of values signifies diagenetic overprint. Most of our data falls within the Aptian ESC (Fig. 8) and have a moderate coefficient of correlation ( $R^2 = 0.5$ ), suggesting a moderate diagenetic impact (Oehlert and Swart, 2014; Swart, 2015). Three datapoints from the Upper Orbitolina Beds (Mortier Tunnel), the Lumachelle I and the Lumachelle II (Les Jarrands) have negative  $\delta^{13}$ C values with  $\delta^{18}\text{O}$  values between -5 and -7 ‰. Such  $\delta^{18}\text{O}$  values fall within or close to the calcite meteoric line of Lohmann (1988), while the negative  $\delta^{13}$ C values may indicate meteoric diagenesis in discrete horizons where cements precipitated from freshwater enriched in soil-respired CO<sub>2</sub>. Field observations confirm this interpretation in the Lumachelle I at Les Jarrands, where karstification associated with the SbAp3 can explain the  $\delta^{13}$ C value of -0.1 ‰. A similar trend was observed in upper Barremian series deposited ca. 55 km further south in the Glandasse Plateau, where Fouke et al. (1996) interpreted negative  $\delta^{13}$ C values as resulting from meteoric diagenesis. There is no evidence for karstification in the Lumachelle II at Les Jarrands, however the quartzarenite lithology of that sample with a negative  $\delta^{13}$ C value may indicate a very shallow environment prone to meteoric diagenesis without the development of a karst surface, and the higher relative contribution of cement in this siliciclastic lithology compared to a limestone. The last datapoint with a negative  $\delta^{13}C$  value (Upper Orbitolina Beds, Mortier Tunnel) belongs to the TST Ap2 where meteoric diagenesis is unlikely to occur (Morad et al., 2012); because the overall trend in  $\delta^{13}$ C values in this TST Ap2 mimics the global trend in  $\delta^{13}$ C values, we conclude that this datapoint may still reflect the original signal. Finally one  $\delta^{18}$ O value lower than -6.50 % (Lumachelle II, Les Jarrands) is associated with a positive  $\delta^{13}\text{C}$  value, and suggests increased rock-fluid interaction during incipient burial that primarily affects  $\delta^{18}$ O values (Choquette and James, 1987). Based on these interpretations, we conclude that our  $\delta^{13}C$  data can serve for chemostratigraphic correlation with series where the expression of the OAE1a is recognized.

The Vercors composite  $\delta^{13}C$  curve (Fig. 10) exhibits several isotope segments diagnostic of the OAE1a: Menegatti et al. (1998) defined a negative  $\delta^{13}C$  spike at the base of the OAE1a (segment C3) followed by a rapid increase in  $\delta^{13}C$  values (C4), a short-lived plateau (C5), and a second increase (C6) before a longer-lasting plateau (C7). These isotope segments are placed alongside the lower Aptian  $\delta^{13}C$  curve for

the Vocontian Basin reproduced from Föllmi et al. (2006) in Fig. 10. In the TST Ap2 (Upper Orbitolina Beds), a negative spike in  $\delta^{13}C$  values down to -0.1~% mimics the C3 segment. Then a rapid increase in  $\delta^{13}C$  values up to 2.32 % at the mfsAp2, a decreasing-upward trend, and a subsequent increasing-upward trend in the HST Ap2 correspond to segments C4, C5 and C7, respectively. The identification of the C3–C7 isotope segments in the Vercors permits placing the onset and unfolding of the OAE1a in the Upper Orbitolina Beds.

The OAE1a has been identified in other peri-Tethyan carbonate platforms after the reliability of the isotope signal was carefully assessed. In the Gargano Promontory of southeastern Italy, Del Viscio et al. (2021) constrained the impact of meteoric diagenesis on lower Aptian series based on  $\delta^{13}$ C vs.  $\delta^{18}$ O cross plots, elemental geochemistry and strontium isotope values, and discarded datapoints associated with exposure surface or dissolution. As a result, these authors recognized isotope segments C2 to C7 that allowed the correlation with other regions from Italy, A major outcome of the study by Del Viscio et al. (2021) is the identification of a Chondrodonta marker bed toward the end of the C2 segment, reflecting the installation of environmental stress directly prior to the OAE1a. This marker bed, however, was not recognized in the south-central Apennines: there, Amodio and Weissert (2017) identified the OAE1a based on the evolution of  $\delta^{13}$ C values, but interpreted the onset of paleoenvironmental instability ca. 1.2 Myr based on the occurrence of Palorbitolina lenticularis and Bacinella-Lithocodium. Further south on the Arabian Plate (Abu Dhabi), Steuber et al. (2022) identified an influence of diagenesis on  $\delta^{18}$ O values, but successfully identified isotope segments C2 to C8 of Menegatti et al. (1998) in their  $\delta^{13}$ C curve. Using time series analysis, Steuber et al. (2022) estimated the duration of the C3 and C4 segments at 104 and 40 kyr, respectively, refining the timing of the onset of the OAE1a.

# 5.2. Quantifying paleoecological change during periods of environmental stress

The impact of paleoenvironmental changes on benthic ecosystems during the early Aptian is documented by changes in the main carbonate-producing organisms in the proto-North Atlantic (Huck et al., 2012), the switch from a photozoan to a heterozoan association in the Helvetic Alps (Föllmi et al., 2006; Stein et al., 2012; Bonvallet et al., 2019), or the collapse in neritic carbonate production coupled with an increased occurrence of pelagic faunas in northern Spain (Millán et al., 2009). In the Gargano Promontory of Italy, Del Viscio et al. (2021) demonstrated that the occurrence of Chondrodonta directly prior to the OAE1a marked the start of deteriorated paleoenvironmental conditions; in particular monospecific beds are found on top of rudistdominated deposits and before a fossil assemblage with orbitolinids and Bacinella-Lithocodium. Thus, the Chondrodonta bedsets described directly below the OAE1a represent the incipient deterioration of environmental conditions and transition from oligotrophic to mesotrophic conditions. The quantification of the degree of biodiversity change associated with the OAE1a could inform on the paleoecological impact of this crisis, however that information is still lacking: Stein et al. (2012) used point counting data to relate the proportion of fossil association with specific paleoecological conditions, but these authors did not leverage these data to quantify how much ecosystems changed as the environment deteriorated.

The identification of isotope segments C3 to C7 in the Upper Orbitolina Beds (see section 5.1) offers a stratigraphic framework to compare the makeup of ecosystems before, during, and after the OAE1a based on point counting data. To unravel biotic associations PCA is applied to point counting data that exclude cement and matrix to only consider rock components with a paleoecological significance. Three clusters of datapoints (Tier 1, Tier 2, and Tier 3; Fig. 9) are interpreted as three distinct biotic associations. Tier 1 includes a fossil assemblage where rudists are the most important biocalcifying photoautotrophic organisms (Schlager, 2005), although Pomar and Hallock

(2008) classify these organisms as suspension feeders based on a comparison with the feeding strategy of modern bivalves. Rudists are grouped with pellets, gastropods, and Bacinella-Lithocodium; the presence of rudist bivalves in Tier 1 indicates a photozoan (Föllmi et al., 2006) to moderately heterozoan assemblage as rudists are thought to have fed on picoplankton from seawater (Pomar and Hallock, 2008). Tier 2 includes the orbitolinid, benthic foraminifera, green algal and miliolid vectors, which indicate a lagoon environment with increased salinity (Schlager, 2005). Tier 3 represents the least diverse assemblage: it includes bivalve, crinoid, bryozoan and non-carbonate grain (quartz and glauconite) vectors, and reflects a heterozoan assemblage more adapted to stressful conditions (Föllmi et al., 2006). The proportion of each tier was quantified in each system tract (pie charts in Fig. 10). In the Upper Urgonian Limestone the proportion of Tier 1 increases from 19 to 48 % to the expense of Tier 2 which proportion decreases from 63 to 27 % in the TST and HST Ap1, respectively. This trend reflects the widespread development of very shallow environments that favored the production of carbonate grains during a keep-up HST (Sarg, 1988), and a slightly improved biodiversity, as deduced from increased <sup>2</sup>D and <sup>0.5</sup>D values (Fig. 10). Sea level seems to control changes in ecological associations during the sequence Ap1. Following on top in the TST Ap2, the increased proportion of Tier 2 (56 %) supports a carbonate production in restricted lagoonal environments with an increased salinity before the rise in sea level accelerates: at L'Achard microfacies F7 and F8 characterize the base on TST Ap2 and transition to microfacies F5 to F3 indicative of more open marine settings near the mfsAp2 (Fig. 4). Hill numbers signal an increase in biodiversity, which is consistent with the installation of more open marine settings. This peak in biodiversity coincides with the C4 segment and with the mfsAp2 (Fig. 10). Moreover based on the abundance and morphology of calcareous nannofossils Erba et al. (2010) concluded that the C4 isotope segment corresponds to the return to conditions more favorable to carbonate production after a period of acidification associated with the C3 segment. Biodiversity changes in the Vercors follow these trends, as lower <sup>0.5</sup>D and <sup>2</sup>D values are reported just prior to and at the C3 isotope segment, respectively, while both biodiversity indices increase during the C4 segment. Thus, paleoecological changes associated with the onset of the OAE1a seem to affect both shallow and deeper marine settings, and may reflect a supraregional trend.

A switch occurred in the HST Ap2: this systems tract is not dominated by Tier 1, but instead Tier 2 represents 49 % of the ecosystem and biodiversity index reaches a minimum value toward its base. In particular <sup>0.5</sup>D and <sup>2</sup>D reach 3.6 and 1.0 at 33.2 m, respectively, coeval with the transition between isotope segments C5 and C6: these minimal values reflect a decreased biodiversity in rare species while the biodiversity of common species is maintained. In this interval carbonate production by benthic foraminifera and green algae makes up 97 % of allochems (sample AS62; see Data repository), and vectors for these organisms overlap Tier 2 datapoints in Fig. 9B. In northern Spain a similar increase in carbonate production by benthic foraminifera is supported by the abundance of orbitolinid-rich facies that occurs in a HST within the OAE1a, and is associated with a pulse of terrigenous continental material (Millán et al., 2011). Our dataset also supports an increased detrital input that starts earlier in the TST Ap2 where  $\%_{terrigenous}$  values increase up to 6.15 % at the mfsAp2. In the Western Swiss Jura several authors (Blanc-Alétru, 1995; Godet et al., 2010; De Kaenel et al., 2020) reported intense erosion and reworking in upper Barremian series where they documented the presence of erosional surfaces, encrusted and bored pebbles, and the presence of late Berriasian-early Valanginian calpionellids in these upper Barremian deposits. The sequence stratigraphic interpretation of these series led Godet et al. (2010) to place these phases of intense reworking within a transgressive systems tract. Similarly the increase in detritism seen in Vercors may reflect enhanced sediment reworking during the increasing rise in sea level. Subsequently %<sub>terrigenous</sub> values decrease down to <1 % in the HST Ap2, before the start of the C7 segment. In the C7 segment (ca. 39 to 55.1 m) %<sub>terrigenous</sub> values higher than 1 % and up to 7.1 % are correlated with a decrease followed by an increase in diversity ( $^{0.5}D = 12.3$  and  $^{2}D = 0.9$ ), and a final decrease in  $^{0.5}D$  values that reach a minimum of 6.2 at the top of the HST Ap2. That relationship may indicate an incipient deterioration in the environment that favored more common and adapted species while rarer species were more sensitive and collapsed. A more significant drop in biodiversity occurs in the Lumachelle I and Lumachelle II: while the diversity of common species maintains a high value of 0.8, the <sup>0.5</sup>D value decreases from 12.3 (base of TST Ap3) to 4.2 in the HST Ap4. A continuously increasing-upward detrital and nutrient input triggered this drop in biodiversity and the dominance of Tier 3 association that represents 74 % of the ecosystem in the TST Ap3. The biodiversity of ecosystems continues to decrease in the Lumachelle II (TST and HST Ap4): Tier 3 makes up 87 (TST Ap4) and 96 % (HST Ap4) of the fossil association, while Hill numbers decrease to 0.5 (<sup>2</sup>D) and 2 (<sup>0.5</sup>D) in the early TST Ap4. To summarize, the biodiversity loss that shallow-marine ecosystems experienced is significant: using Hills numbers <sup>0.5</sup>D we calculated a 46 % decrease in biodiversity from before to after the OAE1a (i.e., from the Upper Urgonian to the Lumachelle), with much of the loss (39 %) occurring from the Upper Orbitolina Beds to the Lumachelle. Factors associated with sea level changes may have contributed to these changes, such as the shift in the depositional environment or variation in detrital and nutrient fluxes (see Section 5.3).

adaption of carbonate ecosystems to changing paleoenvironmental conditions during the early Aptian is documented in other locations of the northern Tethyan margin. In the Helvetic Alps, carbonate production operated a switch from photozoan (Schrattenkalk Formation) and heterozoan (Grünten Member) ecosystems in the early Aptian during the C3 isotope segment. After a phase of drowning (Luitere Bed, C4 to C7 segments) the return of a heterozoan production occurred in the late Aptian (Brisi Beds; Föllmi and Gainon, 2008). Föllmi et al. (2006) postulated that enhanced weathering of continental landmasses and delivery of nutrients, especially phosphorus, drove these changes in benthic carbonate factory, with heterozoan assemblages being better adapted to mesotrophic conditions. This model applies to the Vercors since the large occurrence of Tier 3 in the Lumachelle I and II parallels an increase in P<sub>2</sub>O<sub>5xs</sub> values in the late Aptian, but does not explain the evolution of ecosystems preserved in northwestern Spain (Millán et al., 2011). There, benthic ecosystems experienced a slow down during the C3-C6 segments but the productivity of ecosystems with rudists and branching corals resumed during the C7 segment and afterward. Thus the unfolding of the OAE1a did not affect these ecosystems as much as those in the Vercors and Helvetic Alps, suggesting that local to regional forcing mechanisms modulated the impact of the OAE1a and favored the resilience of ecosystems.

# 5.3. Paleoenvironmental forcing on the paleoecology of the Urgonian platform

The nature of carbonate-producing ecosystems and ecological reorganizations result from the complex interplay of environmental parameters (Mutti and Hallock, 2003; Arnaud-Vanneau, 2005; Schlager, 2005). Recent studies leveraged major and trace element concentrations to reconstruct the quality of seawater at time of deposition, especially when the remobilization of trace elements during early diagenesis is discarded (Swart, 2015). To improve the statistical analysis of geochemical dataset Coimbra et al. (2017) demonstrated that PCA allows assessing the impact of paleoenvironmental parameters during different diagenetic stages or in different lithologies. Following these authors, Godet et al. (2023) applied PCA to elemental and isotope geochemical data to reconstruct Albian depositional environmental conditions in central and west Texas, and demonstrated that periods of enhanced nutrient supply or increased salinity were detrimental to Albian carbonate ecosystems on this region of the Comanche Platform.

Building onto Coimbra et al. (2017) and Godet et al. (2023), two clusters are defined in the PCA plot of geochemical data (Fig. 9A); in the left side, cluster 1 includes Lower Orbitolina Beds, Lumachelle I and Lumachelle II data that align with vectors of detrital and nutrient supply proxies. This relationship indicates sedimentation in an environment with significant detrital and nutrient supply, which is consistent with the frequent occurrence of transgressive microfacies FT rich in quartz and glauconite, the dominance of heterozoan ecosystems with suspension-feeders (crinoids and bryozoans), and the high proportion of Tier 3 (up to 96 % in HST Ap4). In the right side of the plot, Upper Urgonian Limestone and Upper Orbitolina Beds datapoints align with CIA\*, Mn\*, and CaO vectors; this is interpreted as an enhanced carbonate production under a strongly weathering climate and in well-oxygenated water with low nutrient and detrital input during the early Aptian. Further to the north in the southeast of the Paris Basin, Deconinck et al. (2021) interpreted a humid climate prone to enhanced weathering from the presence of kaolinite in the clay fraction of lower Aptian deposits, with most humid conditions coeval with isotope segments C3 to C5 and a decreasing trend in humidity in the C6 and C7 isotope segments. This phase of enhanced weathering could be responsible for higher %terrigenous values in the Upper Orbitolina Beds especially in the C4-C5 segments, while detrital input decreases in the C6 and most of the C7 segments. Further south in Italy, coeval series preserved on the Gargano Promontory were deposited in central Tethys, and record a succession with stromatolites (C3, C4 and most of C5segments), rudists and Bacinella-Lithocodium (end of C5 segment) and orbitolinids and Bacinella-Lithocodium (C6 segment; Del Viscio et al., 2021). These authors concluded that climate instability led to the occurrence of Chondrodonta prior to the OAE1a when nutrient input increased to favor the installation of mesotrophic conditions. In the UAE, rapid depositional environment changes are associated with the OAE1a: Steuber et al. (2022) report a switch from skeletal wackestone to packstone (distal inner ramp; C2 segment) into orbitolinid wackestone to packstone (distal outer ramp), and facies with Bacinella-Lithocodium (distal inner ramp and the low-energy mid-ramp; C3 segment) before the switch to wackestone with Bacinella-Lithocodium (low-energy mid-ramp) and rudist wackestone (proximal outer ramp) in the C4 and C5 segments, respectively. Geochemical data indicate that a drop in carbonate production in the C3 segment results from a decreased pH linked to a maximum in seawater temperature and an increased detrital input. Steuber et al. (2022) concluded that this decreased pH was induced by the short-lived injection of CO<sub>2</sub> into the atmosphere-ocean system that can originate from the Ontong-Java large igneous province.

These changing paleoenvironmental conditions impacted the ecology of benthic ecosystems. Highly diversified photozoan assemblages (Tiers 1 and 2, <sup>0.5</sup>D values up to 14.2) in the Upper Urgonian Limestone and Upper Orbitolina Beds thrived under oligotrophic conditions (P<sub>2</sub>O<sub>5XS</sub> values lower than 0.1), while in the Lumachelle I and II less diversified (0.5D mean value of 5.6 for a maximal value of 8.7) Tier 3 assemblages were deposited under mesotrophic conditions (P2O5XS values up to 0.9). The interpretation of diversity indices in the light of paleoenvironmental reconstruction based on geochemical data illuminates triggering mechanisms for the demise of the Urgonian platform in the Vercors. In the Lumachelle II a significant drop in diversity in the TST Ap4 correlates with a decrease in %terrigenous values while  $P_2O_{5XS}$  values increase from 0.1 to 0.9. This suggests that nutrient supply was the main driver of loss of biodiversity in the TST and HST AP4, and that changes in these two parameters after the OAE1a led to the demise of the platform. The major perturbation of the carbon cycle associated with the OAE1a (C3 isotopic segment) and the subsequent boosted diversity (C4–C5 isotope segments) reflect the ecological reorganization of the Urgonian ecosystems, while the alignment of Lumachelle I and Lumachelle II datapoints with vectors of %terrigenous and P2O5XS (Fig. 9A) indicates that the demise of the platform was triggered by choking by nutrients and, to a lesser extent, detrital particles linked to climate change.

# 6. Conclusions

The detailed study of the lower Aptian series from the Vercors region of southern France provides insights into the potential of resilience of carbonate ecosystems subjected to super greenhouse conditions. The record of the OAE1a is identified in Vercors based on variations in  $\delta^{13}$ C values; the recognition of isotope segments C3 and C4 places the onset of the OAE1a just prior to the mfsAp2 of the early Aptian after the end of deposition of rudist-bearing, Urgonian limestones, while the identification of isotope segments C5 to C7 helps locate the rest of the OAE1a in the TST of the sequence Ap2.

Our multidisciplinary dataset helps constrain and quantify the kind of ecological adjustments ecosystems experienced, and identify the main trigger for these changes. Our analysis of thin sections demonstrates that the unfolding of the OAE1a is associated with an ecological adjustment of benthic ecosystems that produced carbonate typical of a photozoan assemblage throughout the OAE1a, with a higher proportion of ecosystems with green algae, benthic foraminifera, and stromatolites in the C5–C7 segments. This switch is associated with an incipient decrease in biodiversity and parallels the adaptation of ecosystems toward a heterozoan assemblage more adapted to higher detrital and nutrient supplies. We identify detrital input as the first trigger for paleoecological change in the aftermath of the OAE1a while nutrient supply in the late Aptian pushed the platform into a phase of drowning. This paleoenvironmental evolution is a consequence of climate change and increased weathering that are also documented in nearby regions.

Our approach that combines geochemical, petrographic data and their statistical analysis permits us to finetune the succession of paleoecological changes induced by major paleoenvironmental changes such as the OAE1a. The multidisciplinary nature of our dataset provides a comprehensive view of paleoenvironmental perturbations and paleoecological adaptations linked to climate change. The application of our workflow to locations that preserve the record of the OAE1a under different paleolatitudes may help untangle how local and global paleoenvironmental changes shaped the potential of resilience of carbonate ecosystems. Moreover our workflow has the potential to be applied to other locations and/or time periods to complete our understanding of biotic responses to climate changes at different time and spatial scales.

## **Funding**

This work was support by the U.S. National Science Foundation (EAR 1847885, CAREER award to A. Godet).

# **CRediT authorship contribution statement**

**Alexis Godet:** Writing – review & editing, Writing – original draft, Supervision, Project administration, Methodology, Investigation, Funding acquisition, Formal analysis, Data curation, Conceptualization. **Jacob Byerly:** Writing – review & editing, Investigation, Formal analysis. **Matthew Bourdon:** Writing – review & editing, Investigation, Data curation. **Marina Suarez:** Writing – review & editing, Investigation, Data curation.

# **Declaration of competing interest**

The authors declare the following financial interests/personal relationships which may be considered as potential competing interests: Alexis Godet reports financial support was provided by National Science Foundation. If there are other authors, they declare that they have no known competing financial interests or personal relationships that could have appeared to influence the work reported in this paper.

# Acknowledgments

We thank Annie Arnaud-Vanneau, Lucie Bonvallet (Association Dolomieu) and Brahimsamba Bomou (University of Lausanne) for their

help in the field, and Claudia Baumgartner (University of Lausanne) for granting access to the microscope to scan thin sections. Tiffany Barker-Edwards, Korei Patterson, and Wesley Nash (UTSA) contributed to the point counting of thin sections. The comments by Editor-in-Chief Catherine Chagué and two anonymous reviewers greatly improved the quality of this manuscript.

# **Data availability**

Geochemical and point counting data of Aptian series from Vercors, France are available online through Mendeley Data: Godet, Alexis (2023), "Geochemical and point counting analysis data of Aptian series from Vercors, France", Mendeley Data, V1, doi: 10.17632/czzy824tcy.1.

This dataset includes results of the analysis of 110 samples from four outcrops from the Vercors region of southern France. Samples are dated to the early and late Aptian, Early Cretaceous. Samples were processed for elemental and isotope geochemistry using X-ray fluorescence spectrometry and isotope ratio mass spectrometry, respectively. Point counting analysis was performed using scanned whole thin sections loaded into JMicroVision; 250 points were counted in each thin section.

#### References

Amodio, S., Weissert, H., 2017. Palaeoenvironment and palaeoecology before and at the onset of Oceanic Anoxic Event (OAE)1a: reconstructions from Central Tethyan archives. Palaeogeography, Palaeoclimatology, Palaeoecology 479, 71–89.

Arnaud, H., 2005a. Sequence stratigraphy interpretation. In: Adatte, T., Arnaud-Vanneau, A., Arnaud, H., Blanc-Alétru, M.-C., Bodin, S., Carrio-Schaffhauser, E., Föllmi, K.B., Godet, A., Raddadi, M.C., Vermeulen, J. (Eds.), The Hauterivian–Lower Aptian sequence Stratigraphy From Jura Platform to Vocontian Basin: A Multidisciplinary Approach. Géologie Alpine, pp. 174–179.

Arnaud, H., 2005b. The South-East France Basin (SFB) and its Mesozoic evolution. In:
Adatte, T., Arnaud-Vanneau, A., Arnaud, H., Blanc-Alétru, M.-C., Bodin, S., CarrioSchaffhauser, E., Föllmi, K.B., Godet, A., Raddadi, M.C., Vermeulen, J. (Eds.), The
Hauterivian-Lower Aptian Sequence Stratigraphy From Jura Platform to Vocontian
Basin: A Multidisciplinary Approach. Géologie Alpine, pp. 5–28.

Arnaud-Vanneau, A., 1980. Micropaléontologie, paléoécologie et sédimentologie d'une plate-forme carbonatée de la marge passive de la Téthys: l'Urgonien du Vercors septentrional et de la Chartreuse (Alpes occidentales). Géologie Alpine Grenoble Mémoire H.S. 11 (874 pp., in French, with English abstract).

Arnaud-Vanneau, A., 2005. Environmental controls on tropical carbonate platform. In:
Adatte, T., Arnaud-Vanneau, A., Arnaud, H., Blanc-Alétru, M.-C., Bodin, S., CarrioSchaffhauser, E., Föllmi, K.B., Godet, A., Raddadi, M.C., Vermeulen, J. (Eds.), The
Hauterivian-Lower Aptian Sequence Stratigraphy From Jura Platform to Vocontian
Basin: A Multidisciplinary Approach. Géologie Alpine, pp. 29–38.

Arnaud-Vanneau, A., Arnaud, H., 1990. Hauterivian to Lower Aptian carbonate shelf sedimentation and sequence stratigraphy in the Jura and northern Subalpine chains (southeastern France and Swiss Jura). In: Tucker, M.E., Wilson, J.L., Crevello, P.D., Sarg, J.R., Read, J.F. (Eds.), Carbonate Platforms: Facies, Sequences and Evolution. IAS Special Publication. Blackwell Scientific Publications, pp. 203–233.

Arnaud-Vanneau, A., Arnaud, H., 2005. Carbonate facies and microfacies of the Lower Cretaceous carbonate platforms. In: Adatte, T., Arnaud-Vanneau, A., Arnaud, H., Blanc-Alétru, M.-C., Bodin, S., Carrio-Schaffhauser, E., Föllmi, K.B., Godet, A., Raddadi, M.C., Vermeulen, J. (Eds.), The Hauterivian–Lower Aptian Sequence Stratigraphy From Jura Platform to Vocontian Basin: A Multidisciplinary Approach. Géologie Alpine, pp. 39–68.

Arnaud-Vanneau, A., Arnaud, H., Carrio-Schaffhauser, E., Raddadi, M.C., 2005. Urgonian deposits and Barremian–early Aptian sequence stratigraphy in the Vercors massif. In: Adatte, T., Arnaud-Vanneau, A., Arnaud, H., Blanc-Alétru, M.-C., Bodin, S., Carrio-Schaffhauser, E., Föllmi, K.B., Godet, A., Raddadi, M.C., Vermeulen, J. (Eds.), The Hauterivian–Lower Aptian Sequence Stratigraphy From Jura Platform to Vocontian Basin: A Multidisciplinary Approach. Géologie Alpine, pp. 97–126.

Arnaud-Vanneau, A., Arnaud, H., Adatte, T., Godet, A., 2021. Depositional geometries in Barremian platform carbonates from the southeastern France. In: Wright, V.P., Porta, G. Della, Samankassou, E. (Eds.), IAS Field Guide 3 "Exceptionally Exposed Carbonate Outcrops". SEPM, pp. 481–513.

Bellanca, A., Claps, M., Erba, E., Masetti, D., Neri, R., Premoli Silva, I., Venezia, F., 1996. Orbitally induced limestone/marlstone rhythms in the Albian–Cenomanian Cismon section (Venetian region, northern Italy): sedimentology, calcareous and siliceous plankton distribution, elemental and isotope geochemistry. Palaeogeography Palaeoclimatology Palaeoecology 126, 227–260.

Blanc-Alétru, M.-C., 1995. Importance des discontinuités dans l'enregistrement sédimentaire de l'Urgonien jurassien. Micropaléontologie, sédimentologie, minéralogie et stratigraphie séquentielle. Géologie Alpine Mémoire HS n°24 (299 pp., in French, with English abstract).

Bonvallet, L., Arnaud-Vanneau, A., Arnaud, H., Adatte, T., Spangenberg, J.E., Stein, M., Godet, A., Föllmi, K.B., 2019. Evolution of the Urgonian shallow-water carbonate platform on the Helvetic shelf during the late Early Cretaceous. Sedimentary Geology 387, 18–56.

- BRGM, 2024. Geological map of Isère, 1/50,000 scale. https://infoterre.brgm.fr/page/telechargement-cartes-geologiques. (Accessed 3 October 2024).
- Carannante, G., Esteban, M., Milliman, J.D., Simone, L., 1988. Carbonate lithofacies as paleolatitude indicators: problems and limitations. In: Nelson, C.S. (Ed.), Nontropical Shelf Carbonates Modern and Ancient. Sedimentary Geology, pp. 333–346.
- Choquette, P.W., James, N.P., 1987. Diagenesis # 12. Diagenesis in limestones 3. The deep burial environment. Geoscience Canada 14. 3–35.
- Coimbra, R., Horikx, M., Huck, S., Heimhofer, U., Immenhauser, A., Rocha, F., Dinis, J., Duarte, LV., 2017. Statistical evaluation of elemental concentrations in shallowmarine deposits (Cretaceous, Lusitanian Basin). Marine and Petroleum Geology 86, 1029–1046
- Cramer, B.D., Jarvis, I., 2020. Chapter 11 carbon isotope stratigraphy. In: Gradstein, F.M., Ogg, J.G., Schmitz, M.D., Ogg, G.M. (Eds.), Geologic Time Scale 2020. Elsevier, pp. 309–343.
- Daly, A.J., Baetens, J.M., De Baets, B., 2018. Ecological diversity: measuring the unmeasurable. Mathematics 7, 119. https://doi.org/10.3390/math6070119.
- De Kaenel, E., Mojon, P.-O., Pictet, A., 2020. New biostratigraphical data (calcareous nannofossils, ammonites) and Early to Late Barremian transition in the Urgonien Jaune facies and Marnes de la Russille complex of the Swiss Jura Mountains. Swiss Journal of Palaeontology 139 (43 pp.).
- Dean, W.E., 1974. Determination of carbonate and organic matter in calcareous sediments and sedimentary rocks by loss on ignition: comparison with other methods. Journal of Sedimentary Petrology 44, 242–248.
- Deconinck, J.-F., Boué, D., Amédro, F., Baudin, F., Bruneau, L., Huret, E., Landrein, P., Moreau, J.-D., Santo ni, A.L., 2021. First record of early Aptian Oceanic Anoxic Event 1a from the Paris Basin (France) climate signals on a terrigenous shelf. Cretaceous Research 125, 104846. https://doi.org/10.1016/j.cretres.2021.104846.
- Del Viscio, G., Frijia, G., Posenato, R., Singh, P., Lehrmann, D.J., Payne, J.L., Al-Ramadan, K., Struck, U., Jochum, K.P., Morsilli, M., 2021. Proliferation of Chondrodonta as a proxy of environmental instability at the onset of OAE1a: insights from shallow-water limestones of the Apulia Carbonate Platform. Sedimentology 68, 3191–3227.
- Dunham, R.J., 1962. Classification of carbonate rocks according to depositional texture. In: Ham, W.E. (Ed.), Classification of Carbonate Rocks—A Symposium. American Association of Petroleum Geologists, pp. 108–121.
- Engelke, J., Linnert, C., Niebuhr, B., Schnetger, B., Brumsack, H.-J., Mutterlose, J., Wilmsen, M., 2018. Tracking Late Cretaceous environmental change: geochemical environment of the upper Campanian to lower Maastrichtian chalks at Kronsmoor, northern Germany. Cretaceous Research 84, 323–339.
- Erba, E., Bottini, C., Weissert, H.J., Keller, C.E., 2010. Calcarous nannoplankton response to surface-water acidification around Oceanic Anoxic Event 1a. Science 329, 428–432.
- Föllmi, K.B., Gainon, F., 2008. Demise of the northern Tethyan Urgonian carbonate platform and subsequent transition towards pelagic conditions: the sedimentary record of the Col de la Plaine Morte area, central Switzerland. Sedimentary Geology 205, 142–159.
- Föllmi, K.B., Godet, A., Bodin, S., Linder, P., 2006. Interactions between environmental change and shallow-water carbonate build-up along the northern Tethyan margin and their impact on the early Cretaceous carbon-isotope record. Paleoceanography 21 (Suppl. PA4211) (16 pp.).
- Fouke, B.W., Everts, A.-J.W., Zwart, E.W., Schlager, W., Smalley, P.C., Weissert, H., 1996. Subaerial exposure unconformities on the Vercors carbonate platform (SE France) and their sequence stratigraphic significance. In: Howell, J.A., Aitken, J.F. (Eds.), High Resolution Sequence Stratigraphy: Innovations and Applications. The Geological Society, London, pp. 295–320.
- Godet, A., 2013. Drowning unconformities: palaeoenvironmental significance and involvement of global processes. Sedimentary Geology 293, 45–66.
- Godet, A., Föllmi, K.B., Bodin, S., de Kaenel, E., Matera, V., Adatte, T., 2010. Stratigraphic, sedimentological and palaeoenvironmental constraints on the rise of the Urgonian platform in the western Swiss Jura. Sedimentology 57, 1088–1125.
- Godet, A., Suarez, M.B., Price, D., Lehrmann, D.J., Adams, T., 2023. Paleoenvironmental constraints on shallow-marine carbonate production in central and West Texas during the Albian (Early Cretaceous). Cretaceous Research 144, 105462. https://doi.org/10.1016/j.cretres.2022.105462.
- Gradstein, F.M., Ogg, J.G., Schmitz, M.D., Ogg, G.M. (Eds.), 2020. Geologic Time Scale 2020. Elsevier (1357 pp.).
- Herrle, J.O., Kößler, P., Friedrich, O., Erlenkeuser, H., Hemleben, C., 2004. High-resolution carbon isotope records of the Aptian to Lower Albian from SE France and the Mazagan Plateau (DSDP Site 545): a stratigraphic tool for paleoceanographic and paleobiologic reconstruction. Earth and Planetary Science Letters 218, 149–161.
- Hfaiedh, R., Arnaud Vanneau, A., Godet, A., Arnaud, H., Zghal, I., Ouali, J., Latil, J.-L., Jallali, H., 2013. Biostratigraphy and palaeoenvironmental evolution of the Aptian succession at Jebel Bir Oum Ali (Northern Chain of Chotts, South Tunisia). Cretaceous Research 46, 177–207.
- Huck, S., Heimhofer, U., Immenhauser, A., 2012. Early Aptian algal bloom in a neritic proto-North Atlantic setting: Harbinger of global change related to OAE1a? GSA Bulletin 124, 1810–1825.
- Huck, S., Stein, M., Immenhauser, A., Skelton, P.W., Christ, N., Föllmi, K.B., Heimhofer, U., 2014. Response of proto-North Atlantic carbonate-platform ecosystems to OAE1arelated stressors. Sedimentary Geology 313, 15–31.
- James, N.P., 1997. The cool-water carbonate depositional realm. In: James, N.P., Clarke, J.A.D. (Eds.), Cool-water Carbonates. Society for Sedimentary Geology, Tulsa, Oklahoma, pp. 1–20.
- Lees, A., Buller, A.T., 1972. Modern temperate-water and warm-water shelf carbonate sediments contrasted. Marine Geology 13, 1767–1773.

- Lohmann, K.C., 1988. Geochemical patterns of meteoric diagenetic systems and their application to studies of paleokarst. In: James, N.P., Choquette, P.W. (Eds.), Paleokarst. Springer-Verlag, New-York Berlin Heidelberg London Paris Tokyo, pp. 58–80.
- Masse, J.-P., Bellion, Y., Benkhelil, J., Dercourt, J., Guiraud, R., Ricou, L.E., 1993. Lower Aptian palaeoenvironments (114 to 112 Ma). In: Dercourt, J., Ricou, L.E., Vrielynck, B. (Eds.), Atlas Tethys Palaeoenvironmental Maps. Maps. Gauthier-Villars, Paris (pp. BEICIP-FRANLAB, Rueil-Malmaison).
- McLennan, S.M., 1993. Weathering and global denudation. The Journal of Geology 101, 295–303
- Menegatti, A.P., Weissert, H., Brown, R.S., Tyson, R.V., Farrimond, P., Strasser, A., Caron, M., 1998. High-resolution d<sup>13</sup>C stratigraphy through the early Aptian "Livello Selli" of the Alpine Tethys. Paleoceanography 13, 530–545.
- Millán, M.I., Weissert, H.J., Fernandez-Meridiola, P.A., Garcia-Mondejar, J., 2009. Impact of Early Aptian carbon cycle perturbations on evolution of a marine shelf system in the Basque-Cantabrian Basin (Aralar, N Spain). Earth and Planetary Science Letters 287, 392-401
- Millán, M.I., Weissert, H.J., Owen, H., Fernàndez-Mendiola, P.A., Garcia-Mondejar, J., 2011. The Madotz Urgonian platform (Aralar, northern Spain): paleoecological changes in response to Early Aptian global environmental events. Palaeogeography, Palaeoclimatology, Palaeoecology 312, 167–180.
- Morad, S., Ketzer, J.M., De Ros, L.F., 2012. Linking diagenesis to sequence stratigraphy: an integrated tool for understanding and predicting reservoir quality distribution. In: Morad, S., Ketzer, J.M., De Ros, L.F. (Eds.), Linking Diagenesis to Sequence Stratigraphy. International Association of Sedimentologists Special Publication. John Wiley & Sons, Ltd., pp. 1–36.
- Morard, R., Hassenrück, C., Greco, M., Fernandez-Guerra, A., Rigaud, S., Douady, C.J., Kucera, M., 2022. Renewal of planktonic foraminifera diversity after the Cretaceous Paleogene mass extinction by benthic colonizers. Nature Communications 13, 7135. https://doi.org/10.1038/s41467-022-34794-5.
- Mutti, M., Hallock, P., 2003. Carbonate systems along nutrient and temperature gradients: some sedimentological and geochemical constraints. International Journal of Earth Science (Geol Rundsch) 92, 465–475.
- Najarro, M., Rosales, I., Martín-Chivelet, J., 2011. Major palaeoenvironmental perturbation in an Early Aptian carbonate platform: prelude of the Oceanic Anoxic Event 1a? Sedimentary Geology 235, 50–71.
- Nesbitt, H.W., Young, G.M., 1982. Early Proterozoic climates and plate motions inferred from major element chemistry of lutites. Nature 299, 715–717.
- O'Brien, C.L., Robinson, S.A., Pancost, R.D., Sinninghe Damsté, J.S., Schouten, S., Lunt, D.J., Alsenz, H., Bornemann, A., Bottini, C., Brassell, S.C., Farnsworth, A., Forster, A., Huber, B.T., Inglis, G.N., Jenkyns, H.C., Linnert, C., Littler, K., Markwick, P., McAnena, A., Mutterlose, J., Naafs, B.D.A., Püttmann, W., Sluijs, A., van Helmond, N.A.G.M., Vellekoop, J., Wagner, T., Wrobel, N.E., 2017. Cretaceous sea-surface temperature evolution: constraints from TEX86 and planktonic foraminiferal oxygen isotopes. Earth-Science Reviews 172, 224–247.
- Oehlert, A.M., Swart, P.K., 2014. Interpreting carbonate and organic carbon isotope covariance in the sedimentary record. Nature Communications 5, 4672. https://doi.org/10.1038/ncomms5672.
- Philip, J., 2003. Peri-Tethyan neritic carbonate areas: distribution through time and driving factors. Palaeogeography, Palaeoclimatology, Palaeoecology 196, 19–37.
- Pomar, L., Hallock, P., 2008. Carbonate factories: a conundrum in sedimentary geology. Earth-Science Reviews 87, 134–169.
- Rameil, N., Immenhauser, A., Warrlich, G., Hillgärtner, H., Droste, H.J., 2010. Morphological patterns of Aptian Lithocodium–Bacinella geobodies: relation to environment and scale. Sedimentology 57, 883–911.
- Sarg, J.F., 1988. Carbonate sequence stratigraphy. In: Wilgus, C.K., Ross, C.A., Posamentier, H. (Eds.), Sea-level Changes — An Integrated Approach, pp. 155–181.
- Schlager, W., 2005. carbonate sedimentology and sequence stratigraphy. Concepts in Sedimentology and Paleontology. vol. 8. SEPM, Tulsa, Oklahoma, USA (203 pp.).
- Schlanger, S.O., Jenkyns, H.C., 1976. Cretaceous oceanic anoxic events: causes and consequences. Geologie en Mijnbouw 55, 179–184.
- Skelton, P., Gili, E., 2012. Rudists and carbonate platforms in the Aptian: a case study on biotic interactions with ocean chemistry and climate. Sedimentology 59, 81–117.
- Stein, M., Arnaud-Vanneau, A., Adatte, T., Fleitmann, D., Spangenberg, J.E., Föllmi, K.B., 2012. Palaeoenvironmental and palaeoecological change on the northern Tethyan carbonate platform during the Late Barremian to earliest Aptian. Sedimentology 59, 939–963.
- Steuber, T., Alsuwaidi, M., Hennhoefer, D., Sulieman, H., AlBlooshi, A., McAlpin, T.D., Shebl, H., 2022. Environmental change and carbon-cycle dynamics during the onset of Cretaceous oceanic anoxic event 1a from a carbonate-ramp depositional system, Abu Dhabi. U.A.E. Palaeogeography, Palaeoclimatology, Palaeoecology 602, 111086. https://doi.org/10.1016/j.palaeo.2022.111086.
- Steuber, T., Löser, H., Mutterlose, J., Parente, M., 2023. Biogeodynamics of Cretaceous marine carbonate production. Earth-Science Reviews 238, 104341. https://doi.org/ 10.1016/j.earscirev.2023.104341.
- Swart, P.K., 2015. The geochemistry of carbonate diagenesis: the past, present and future. Sedimentology 62, 1233–1304.
- Wedepohl, K.H., 1991. The composition of the Upper Earth's crust and the natural cycles of selected mateals. Metal in natural raw materials. Natural resources. In: Merian, E. (Ed.), Metals and Their Compounds in the Environment. VCH Verlagdgesellschaft mbH, Weinheim - New York - Basel - Cambridge, pp. 3–18.
- Weissert, H., 1989. C-isotope stratigraphy, a monitor of paleoenvironmental change: a case study from the Early Cretaceous. Surveys in Geophysics 10, 1–61.
- Weissert, H., McKenzie, J., Hochuli, P., 1979. Cyclic anoxic events in the Early Cretaceous Tethys Ocean. Geology 7, 147–151.